The Astrophysical Journal, 837:11 (19pp), 2017 March 1 https://doi.org/10.3847/1538-4357/837/1/11

A High Space Density of Luminous Lyα Emitters at $z \sim 6.5$

Micaela B. Bagley[1], Claudia Scarlata[1], Alaina Henry[2], Marc Rafelski[2], Matthew Malkan[3], Harry Teplitz[4], Y. Sophia Dai[4], Ivano Baronchelli[4], James Colbert[4], Michael Rutkowski[5], Vihang Mehta[1], Alan Dressler[6], Patrick McCarthy[6], Andrew Bunker[7], Hakim Atek[8], Thibault Garel[9], Crystal L. Martin[10], Nimish Hathi[11,2], and Brian Siana[12]
[1] Minnesota Institute for Astrophysics, University of Minnesota, Minneapolis, MN 55455, USA
[2] Space Telescope Science Institute, Baltimore, MD 21218, USA
[3] Department of Physics & Astronomy, University of California, Los Angeles, CA 90095, USA
[4] Infrared Processing and Analysis Center, California Institute of Technology, Pasadena, CA 91125, USA
[5] Stockholm University, Department of Astronomy and Oskar Klein Centre for Cosmoparticle Physics, AlbaNova University Centre, SE-10691, Stockholm, Sweden
[6] Carnegie Observatories, Pasadena, CA 91101, USA
[7] Department of Physics, University of Oxford, Oxford, UK
[8] Laboratoire dAstrophysique, Ecole Polytechnique Fédérale de Lausanne, Observatoire de Sauverny, CH-1290 Versoix, Switzerland
[9] Univ Lyon, Univ Lyon1, Ens de Lyon, CNRS, Centre de Recherche Astrophysique de Lyon UMR5574, F-69230, Saint-Genis-Laval, France
[10] Department of Physics, University of California, Santa Barbara, CA 93106, USA
[11] Laboratoire d'Astrophysique de Marseille, Marseille, France
[12] Department of Physics, University of California, Riverside, CA 92521, USA
Received 2016 October 13; revised 2016 December 14; accepted 2017 January 10; published 2017 February 27

Abstract

We present the results of a systematic search for Lyα emitters (LAEs) at $6 \lesssim z \lesssim 7.6$ using the *HST* WFC3 Infrared Spectroscopic Parallel (WISP) Survey. Our total volume over this redshift range is $\sim 8 \times 10^5$ Mpc^3, comparable to many of the narrowband surveys despite their larger area coverage. We find two LAEs at $z = 6.38$ and 6.44 with line luminosities of $L_{\mathrm{Ly}\alpha} \sim 4.7 \times 10^{43}$ erg s^{-1}, putting them among the brightest LAEs discovered at these redshifts. Taking advantage of the broad spectral coverage of WISP, we are able to rule out almost all lower-redshift contaminants. The WISP LAEs have a high number density of 7.7×10^{-6} Mpc^{-3}. We argue that the LAEs reside in megaparsec-scale ionized bubbles that allow the Lyα photons to redshift out of resonance before encountering the neutral intergalactic medium. We discuss possible ionizing sources and conclude that the observed LAEs alone are not sufficient to ionize the bubbles.

Key words: cosmology: observations – galaxies: high-redshift

1. Introduction

The dark ages that followed recombination ended with the appearance of metal-free stars and the subsequent formation of numerous low-mass, metal-poor galaxies. The collective ionizing background from these newly forming galaxies is thought to be responsible for the reionization of the diffuse hydrogen in the intergalactic medium (IGM) between $z \sim 6.5$ and $z \sim 10$ (e.g., Fan et al. 2006; Robertson & Ellis 2012; Madau & Haardt 2015; Planck Collaboration et al. 2016a). The progression of the reionization history depends on the nature of these first sources—their number densities, luminosities, clustering, and production rates of ionizing photons—which is currently the subject of considerable observational and theoretical efforts.

The evolving neutral hydrogen fraction in the IGM can be constrained using observations of the Lyα output from galaxies around the end of reionization. Lyα photons are produced by a resonant transition and so are sensitive to the presence of even a small fraction of neutral hydrogen. In particular, a drop in both the number density of Lyα emitters (LAEs) and in the fraction of LAEs among star-forming galaxies is expected at $z \gtrsim 6$ due to the increase in neutral hydrogen in the IGM.

Observational studies comparing the $z \simeq 5.7$, $z \simeq 6.5$, and $z \geqslant 7$ Lyα luminosity functions (LFs) have so far reached inconsistent conclusions. Some find a deficit with increasing redshift in the number density of LAEs either at the bright end of the LF (e.g., Kashikawa et al. 2011), the faint end of the LF (e.g., Matthee et al. 2014, 2015), or at all luminosities (Konno et al. 2014). The differences in completeness associated with each survey could contribute to this disagreement. For example, the large discrepancy between the faint ends of the Lyα LFs of Kashikawa et al. (2011) and Hu et al. (2010) is likely due to the former's deeper spectroscopic observations. Cosmic variance may also contribute to the discrepancies at the bright end. Recent and ongoing narrowband surveys are covering much larger areas than previous surveys. For example, Matthee et al. (2015) and Santos et al. (2016) present the results of their 7 sq. degree survey, while Hu et al. (2016) report on findings in 3 sq. degrees of their 24 sq. degree survey. On the other hand, Hu et al. (2010) covered just 1.16 sq. degrees, and Kashikawa et al. (2011) went very deep in a single pointing of $\sim$0.25 sq. degrees. It is possible that the older surveys, more susceptible to cosmic variance because of their narrow redshift windows, did not cover volumes large enough to probe the true variation in the number densities of these rare, brightest objects.

While observational issues do exist, the observed disagreement could also be caused by real astrophysical phenomena. Reionization is not expected to proceed at the same rate on all scales (e.g., Mesinger & Furlanetto 2008; Zheng et al. 2011; Treu et al. 2012), but rather to be a patchy and inhomogeneous process depending on the luminosity of ionizing sources and the galaxy clustering properties. The effect of both luminosity and clustering is to produce large ionized bubbles (on scales of a few megaparsecs, depending on the exact luminosity) that allow Lyα photons to redshift out of resonance before encountering the IGM. Therefore, we may expect the most luminous LAEs to be visible out to earlier times. Conversely, it will take the fainter galaxies longer to ionize bubbles large

enough to allow Lyα photons to escape (e.g., Ono et al. 2012; Matthee et al. 2015; Stark et al. 2016). Additionally, around luminous sources or highly clustered regions, we may expect an enhancement in the number density of galaxies showing Lyα in emission (Castellano et al. 2016).

Small sample sizes and contamination by lower-redshift interlopers are both major concerns in high-redshift LAE searches. Tilvi et al. (2010) and Krug et al. (2012) claim to find evidence that the number density of LAEs either does not evolve or slightly increases from $z=$ 5.7 to 7.7. These results were likely due to contamination. Indeed, the follow-up observations of Faisst et al. (2014) find no Lyα emission in the spectrum of either LAE candidate from Krug et al. (2012). Due to the challenges of performing ground-based narrowband searches at $z > 7$, the majority of candidates targeted for spectroscopic confirmation are identified from broadband colors indicative of a Lyman break (e.g., Pentericci et al. 2011, 2014; Vanzella et al. 2011; Ono et al. 2012; Schenker et al. 2012). Such "dropout" samples, however, can suffer from large contamination fractions, especially for fainter galaxies (e.g., Dickinson et al. 2004; Stanway et al. 2008). Moreover, as surveys for ultrafaint LAEs have shown (Dressler et al. 2011, 2015; Henry et al. 2012), continuum-based searches may miss significant fractions of faint galaxies that are important for reionizing the IGM.

Spectroscopic surveys with *HST*'s WFC3/IR grism are well suited to address the still-uncertain evolution of the bright end of the Lyα LF at $z \sim$ 6–7. The WFC3 Infrared Spectroscopic Parallel (WISP, PI: M. Malkam, Atek et al. 2010) Survey covers more than 1700 arcmin^2 in 386 uncorrelated fields. Here we present the results of a search for $z \sim$ 6–7 galaxies in the 48 deepest WISP fields available, covering $\sim$160 arcmin^2. We compensate for the small area by covering a broad redshift range ($6 \lesssim z \lesssim 7.6$), enabling us to probe a volume of 8×10^5 Mpc^3 at $z > 6$. We are also able to rule out almost all lower-redshift contaminants thanks to the broad spectral coverage of the WISP survey.

This paper is organized as follows. In Section 2 we describe our WISP observations and data reduction. We present the selection of $z > 6$ LAEs in Section 3 and the expected contamination fraction in Section 4. We present our results in Section 5 and discuss the implications in Section 6. Throughout this paper we assume a cosmology with $\Omega_0 = 0.3$, $\Omega_\Lambda = 0.7$, and $H_0 = 70$ km s^{-1} Mpc^{-1}. All magnitudes are expressed in the AB system (Oke & Gunn 1983).

2. Observations: The WISP Survey

The WISP Survey (PI: M. Malkan, Atek et al. 2010) is a near-infrared slitless grism spectroscopic program that efficiently accrues WFC3[13] data while other *HST* instruments are in use. Observations with either the Cosmic Origins Spectrograph (COS; Froning & Green 2009) or the Space Telescope Imager and Spectrograph (STIS; Kimble et al. 1998) require long integrations of a single pointing. During such integrations, WFC3 (Kimble et al. 2008) can be used to observe targets offset by 5.′5 and 4.′75 from the COS and STIS primary targets, respectively. WFC3 has a field of view of $123'' \times 134''$ and $162'' \times 162''$ for the IR (0.″13/pixel) and UVIS (0.″04/pixel) cameras, respectively. To date the WISP survey has observed 386 fields collectively covering more than 1700 arcmin^2.

We use both of WFC3's IR grisms: G_{102} (0.8–1.1 μm, $R \sim 210$) and G_{141} (1.07–1.7 μm, $R \sim 130$). To aid in extracting the spectra from the slitless grism images, the WISP fields were also observed in direct imaging mode with filters chosen to match the grism spectral coverage: F110W for G_{102} and either F140W or F160W for G_{141}. The WISP observing strategy depends on the length of each parallel opportunity and can therefore vary somewhat from field to field. In general, grism integration times are $\sim$6$\times$ those for the direct images, reflecting the sensitivities in both instrument modes. Of the 386 WISP fields, 117 are also observed with the WFC3 UVIS camera and a subset of the filters F475X, F600LP, F606W, and F814W (see Ross et al. 2016 for details).

All data are reduced with the WFC3 pipeline CALWF3 in combination with custom scripts that account for the undithered, pure-parallel observations (Atek et al. 2010; Ross et al. 2016). The UVIS images are also corrected for the charge transfer efficiency degradation of the WFC3/UVIS detector and processed with customized darks based on the methodology of Rafelski et al. (2015). We use *Source Extractor* (version 2.5, Bertin & Arnouts 1996) for object detection in the direct images and the `aXe` software package (Kümmel et al. 2009) to extract and calibrate the spectra.

The WISP Survey includes a shallow survey of fields observed for one to three continuous orbits and a deep survey of fields observed for four or more continuous orbits. For these deep fields, the integration times in the two grisms are $\sim$5:2 (G_{102} : G_{141}) in order to achieve approximately uniform sensitivity for a line of a given flux. In this paper we consider a subset of the deep survey, consisting of 48 fields ($\sim$160 arcmin^2 [14]) reaching 5σ depths in the IR of $m_{\rm AB} \sim$ 26–26.8 and UVIS 1σ depths of $m_{\rm AB} \geqslant 27$. All these fields were observed with F110W and F160W, hereafter J_{110} and H_{160}, respectively. Of these 48 fields, 21 were observed with both F606W and F814W (V_{606} and I_{814}), and the remaining 27 have only I_{814} imaging. The exposure times and flux limits for the 48 fields are listed in Table 1. In the following sections, we describe the creation of the photometric and emission line catalogs used in this analysis.

2.1. Photometric Catalog

Using AstroDrizzle (Gonzaga et al. 2012), we drizzle the IR direct images onto the UVIS pixel scale (0.″04). We choose 0.″04 because drizzling all images onto the lower-resolution IR pixel scale (0.″13) reduces the depth in the UVIS images, especially for small compact objects. This choice only affects the final drizzled images used for photometry. All other data reduction and cosmic-ray rejection is done on the original pixel scales.

Source detection and photometry are performed with *Source Extractor* in dual image mode using a combined detection image made from all *HST* images of the field. In detail, we first convolve the UVIS images with Gaussian kernels to match the resolution of the H_{160} images. We then construct the detection

[13] http://ww.stsci.edu/hst/wfc3/

[14] The effective grism area of the WISP survey is $\sim$3.3 arcmin^2, rather than the 4.3 arcmin^2 of the WFC3 IR channel. Area on the left side of each field is lost because sources are not covered in the direct images—necessary for wavelength calibration—while area on the right is lost because contaminating zero-order images cannot be identified for the spectra.

Table 1
WISP Fields Used in This Work, Exposure Times, and Depths

Field	t_{G102} (s)	G102[a] (1σ) (erg s^{-1} cm^{-2})	t_{V606} (s)	V_{606}[b] (1σ)	t_{I814} (s)	I_{814} (1σ)	t_{J110} (s)	J_{110} (5σ)	t_{H160} (s)	H_{160} (5σ)
96	28079	5.69×10^{-18}	1500	28.40	1500	27.65	4294	27.39	1765	26.49
256	4218	6.08×10^{-17}	⋯	⋯	1500	27.14	1015	26.20	406	25.34
257	8229	3.30×10^{-17}	900	28.11	1500	27.67	1818	26.86	759	25.84
258	6021	1.45×10^{-17}	⋯	⋯	1500	27.73	1215	26.08	609	25.09
260	7526	8.82×10^{-18}	⋯	⋯	1500	27.70	1365	26.66	609	25.65
261	6021	1.16×10^{-17}	⋯	⋯	1500	27.55	1215	26.28	609	25.57
271	4015	1.92×10^{-17}	⋯	⋯	1500	27.36	809	26.31	406	25.31
288	4218	1.44×10^{-17}	⋯	⋯	1500	27.62	1015	26.48	406	25.43
294	4218	1.36×10^{-17}	⋯	⋯	1500	27.62	1015	26.52	406	25.44
295	4318	1.29×10^{-17}	⋯	⋯	1500	27.57	1015	26.45	406	25.41
296	13544	8.82×10^{-18}	1500	27.85	2500	27.52	2376	26.60	1015	25.90
297	4518	1.20×10^{-17}	⋯	⋯	1500	27.53	1015	26.24	406	25.31
298	11835	1.00×10^{-17}	1200	28.06	2000	27.55	2407	26.16	1015	25.60
300	6921	1.16×10^{-17}	⋯	⋯	1500	27.54	1262	26.11	609	25.61
302	7023	1.40×10^{-17}	900	27.86	1500	27.49	1412	26.69	812	25.73
303	7623	8.09×10^{-18}	900	28.16	1500	27.35	1315	26.28	609	25.62
304	13038	4.22×10^{-17}	1500	28.32	2500	27.94	2960	26.95	1015	25.95
307	7323	1.08×10^{-17}	900	27.81	1500	27.52	1215	26.61	812	25.72
308	4518	1.85×10^{-17}	⋯	⋯	1500	27.67	1015	26.53	406	25.48
309	5315	1.29×10^{-17}	⋯	⋯	1500	27.53	1015	26.52	456	25.60
311	7821	8.82×10^{-18}	⋯	⋯	1500	27.74	1468	26.42	609	25.46
312	5818	1.10×10^{-17}	⋯	⋯	1500	27.56	1165	26.81	609	25.76
313	7226	1.49×10^{-17}	⋯	⋯	1500	27.55	1315	26.82	609	25.68
314	16147	2.84×10^{-17}	1500	28.28	2500	27.81	2901	26.40	1543	26.07
315	6318	1.35×10^{-17}	⋯	⋯	1500	27.60	1218	26.78	609	25.76
317	4518	2.34×10^{-17}	⋯	⋯	1500	27.48	1015	26.40	406	25.45
319	8326	1.40×10^{-17}	2200	28.31	2200	27.76	1621	26.61	609	25.69
320	12732	1.24×10^{-17}	2400	28.23	2400	27.62	2782	26.73	1065	25.88
321	12035	9.65×10^{-18}	2200	28.46	2200	27.80	2154	26.85	887	25.94
324	12135	9.78×10^{-18}	2200	28.14	2200	27.54	2204	26.41	912	25.69
325	9223	3.03×10^{-17}	2400	28.21	2400	27.51	2023	26.78	762	25.78
326	11535	1.27×10^{-17}	1500	28.09	1800	27.55	2126	26.65	859	25.94
333	15941	9.26×10^{-18}	2200	27.24	2200	27.64	2866	26.79	1193	26.05
340	7421	8.30×10^{-18}	2400	28.49	2400	27.81	1721	26.55	709	25.88
341	5921	1.17×10^{-17}	⋯	⋯	1500	27.63	1215	26.01	609	25.55
345	8021	9.03×10^{-18}	2400	28.66	2400	27.78	1421	26.65	609	25.72
347	6015	1.51×10^{-17}	2400	27.99	2400	27.67	1771	26.39	1012	25.83
348	6615	1.13×10^{-17}	⋯	⋯	2000	27.74	1165	26.55	609	25.63
349	5412	9.56×10^{-18}	⋯	⋯	2400	27.76	962	26.33	609	25.68
352	6721	1.19×10^{-17}	⋯	⋯	2000	27.49	1671	26.64	684	25.74
357	9223	1.11×10^{-17}	2400	28.44	2400	27.80	2023	26.48	812	25.75
360	7721	1.08×10^{-17}	⋯	⋯	2400	27.76	1721	26.40	759	25.79
364	6921	1.05×10^{-17}	⋯	⋯	2200	27.85	1318	26.77	609	25.68
368	6518	1.38×10^{-17}	⋯	⋯	2400	27.78	1696	26.80	734	25.92
369	9629	1.10×10^{-17}	2200	28.51	2200	27.77	2276	26.73	759	25.86
371	6618	1.18×10^{-17}	⋯	⋯	2600	27.82	1218	26.61	534	25.47
379	2809	1.13×10^{-17}	⋯	⋯	2400	27.97	1721	26.69	759	25.94
385	2406	1.22×10^{-17}	⋯	⋯	1996	27.55	1165	26.57	609	25.68

Notes.
[a] G_{102} flux limits depend on wavelength with the sensitivity of the grism. Values presented here are at $\lambda = 1$ μm.
[b] Limits are 1σ in UVIS and 5σ in the IR, matching the selection criteria described in Section 3.

image as the weighted average of the images in all four filters:

$$\frac{1}{n}\sum_i \frac{I_i}{\sqrt{w_i}}. \quad (1)$$

Combining the J_{110} and H_{160} images produces a deeper image than either individual filter and enables the detection of additional objects that would be missed by using a single filter for detection. The UVIS images are included in our detection image to ensure that there is adequate coverage of all pixels. As we cannot dither the telescope, we do not have sufficient exposures to cover all IR pixels at the $0\farcs04$ pixel scale. As a result, the IR images drizzled to the UVIS pixel scale contain "bad" pixels that lack the information to have a reliable flux. These pixels have weights of zero, and we have confirmed that they do not affect the photometry.

We run *Source Extractor* twice for each UVIS filter: once on the original, unconvolved image, and once on the image

convolved to match the resolution of H_{160}. The unconvolved UVIS images (at the original resolution) are deeper than those that have been convolved. The photometry calculated on the unconvolved images is therefore used to determine which sources are undetected in the UVIS filters. The photometry from the convolved images is used in calculating galaxy colors. We use circular aperture magnitudes with $r = 0\farcs3 = 7.5$ pixels to measure galaxy colors. All other analysis is done with *Source Extractor*'s `AUTO` elliptical apertures.

2.2. Emission Line Catalog

Emission line candidates are identified using an automatic algorithm that selects groups of contiguous pixels above the continuum. Every candidate is then carefully inspected by two reviewers. This visual inspection is necessary to reject cosmic rays, hot pixels, and other artifacts and sources of contamination that could not be removed during image reduction due to the lack of dithering. In total, 2180 emission line galaxies have been identified in these 48 WISP fields. See Colbert et al. (2013) and Ross et al. (2016) for a detailed description of the WISP line-finding process.

While the WISP Survey is optimized to detect Hα and [O III] emitters at $0.3 < z < 2.4$, it is also well suited for the search for LAEs at $z > 6$. In the WISP emission line catalog, all single emission lines with no visible asymmetry are assumed to be Hα. However, there is the possibility that some of the faintest single-line emitters are actually LAEs at $z \geqslant 6$. Most of the exposure time in the longer WISP parallel opportunities is devoted to G_{102} observations, enabling the grism images to reach the sensitivities necessary for detecting $z > 6$ emission lines. The observed equivalent width (EW) limit of the WISP Survey (40 Å, Colbert et al. 2013) corresponds to a low limit of $\mathrm{EW}_0 = 5.3$ Å in the rest frame of a galaxy at $z = 6.5$. In Section 3, we describe how we select LAE candidates from the single-line emitters in the WISP emission line catalog.

3. Sample Selection

3.1. Choosing the Selection Criteria

The selection criteria, which we present in Section 3.2, aim to select single-line emitters with colors indicative of a Lyman break. We choose the criteria after minimizing the number of lower-z contaminants that enter the LAE sample. To do so, we create a large library of simulated spectral templates based on the models of Bruzual & Charlot (2003). From this library we generate a catalog of colors in the WISP bands for galaxies over $0.1 \leqslant z \leqslant 8.5$. The synthetic catalog is described in Appendix A. We then use the synthetic catalog to determine the effect of varying three parameters: (1) the range of observed emission line wavelengths we consider, (2) the level of flux allowed in I_{814}, and (3) the location of the selection window in color space. In the following sections, we discuss each of these three parameters and their effect on the sample contamination. We define $f_{\text{low-}z}$ as the number of lower-z galaxies selected by our criteria divided by the total number of selected galaxies: $f_{\text{low-}z} = N_{\text{low-}z}/(N_{\text{high-}z} + N_{\text{low-}z})$, where $N_{\text{high-}z}$ is the number of galaxies at $6.00 \leqslant z \leqslant 7.63$. Only lower-$z$ galaxies in very specific redshift ranges can enter the sample and contribute to $N_{\text{low-}z}$ (see Section 4 for details). The contamination fraction we expect for the WISP sample, denoted f_{contam}, is much lower than $f_{\text{low-}z}$ because we can use the broad wavelength coverage and typical emission line ratios from the WISP catalog to exclude lower-redshift interlopers. We discuss f_{contam} in Section 4. Likewise, the recovery fraction, f_{recover}, is defined as the number of high-z galaxies selected by our criteria divided by the total number of high-z galaxies in the full synthetic catalog. The maximum f_{recover} achieved over the full parameter space is 0.9. We choose values for the three parameters that minimize $f_{\text{low-}z}$ while keeping f_{recover} within 10% of this maximum.

3.1.1. Wavelength of Emission

The range of observed wavelengths we consider in selecting single-line emitters determines the range of redshifts we probe for both high-z LAEs and lower-z contaminants. The G_{102} grism covers $0.85 \lesssim \lambda_{\text{obs}} \lesssim 1.13\ \mu$m, corresponding to $6.0 \leqslant z_{\text{Ly}\alpha} \leqslant 8.3$. However, including sources with emission lines across this full wavelength range results in an unacceptable number of contaminants. Additionally, we do not have the grism depth to detect galaxies at $z \gtrsim 8$ (a Lyα luminosity of $\log_{10}(L_{\text{Ly}\alpha}) = 10^{43}$ erg s^{-1} at $z = 8$ has a flux of $\sim 1.3 \times 10^{-17}$ erg s^{-1} cm^{-2}, below the 3σ sensitivities we reach in G_{102}). We therefore apply a wavelength cut in our selection of single-line emitters. We vary this maximum wavelength over $1.0 - 1.13\ \mu$m and find that $\lambda_{\text{obs,max}} = 1.05\ \mu$m results in $f_{\text{recover}} = 0.84$ while $f_{\text{low-}z}$ is just below 0.3.

3.1.2. Flux in I_{814}

A $z > 6$ galaxy may emit enough flux in I_{814} to register a signal at greater than 1σ. For example, the Lyman break in the spectrum of a $z \sim 6.6$ galaxy occurs at $\lambda_{\text{obs}} \sim 9000$ Å, $\sim$1000 Å blueward of the edge of the I_{814} filter. With imaging in at most one additional filter blueward of I_{814}, we cannot confirm that a $z \geqslant 6$ galaxy with some flux in I_{814} has truly dropped out of the optical. The level of I_{814} source flux above the background we allow in selecting candidates will therefore strongly affect the expected contamination fraction. We consider I_{814} detection thresholds in the range $1\sigma - 3\sigma$ and find that 1σ is the best option in terms of recovery and contamination fractions ($f_{\text{recover}} = 0.83$, and $f_{\text{low-}z} = 0.29$). Including galaxies that are nondetections at the 1.5σ level increases the contamination to $f_{\text{low-}z} \sim 0.4$. There are two single-line emitters in the WISP catalog that are nondetections in I_{814} at 1.5σ. We conservatively reject these to avoid contamination from faint, lower-redshift interlopers. We include their spectra and direct image stamps in Appendix B.

3.1.3. Selection Window

Figure 1 shows the color–color plot used to identify $z > 6$ dropout galaxies. In choosing the selection criteria, we vary the shape and size of the color selection window, covering the range indicated by the dashed lines in Figure 1. The red limit in $(J_{110} - H_{160})$ has the largest effect on both f_{recover} and $f_{\text{low-}z}$. We consider windows as red as $(J_{110} - H_{160}) = 1.3$ and choose 0.5 with $f_{\text{recover}} = 0.8$ and $f_{\text{low-}z} = 0.22$. Only 1% of the $z < 6$, UVIS-undetected galaxies in the selection window come from the lower right corner of our selection region. For simplicity, we therefore use a rectangular selection region rather than the more complicated windows used by, for example, Oesch et al. (2010) and Bouwens et al. (2015). The requirement for emission line detection in our sample removes any concern over contamination from this region.

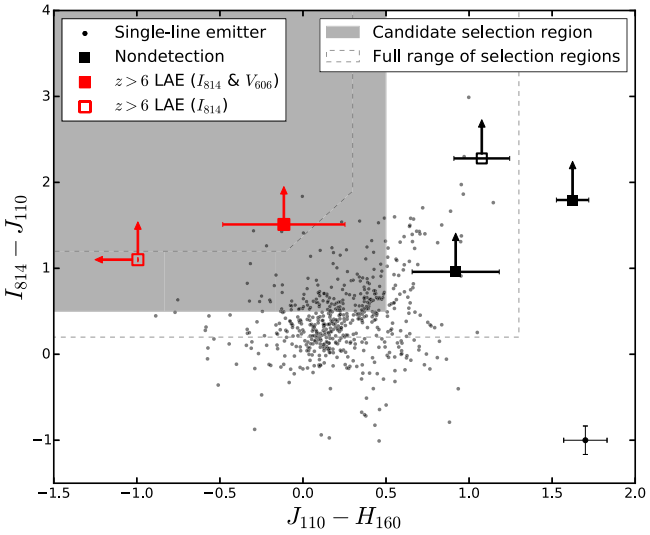

Figure 1. $I_{814} - J_{110}$ vs. $J_{110} - H_{160}$ color–color plot used to identify $z > 6$ dropout galaxies. The gray region shows the candidate selection region. The dashed lines indicate the range of selection regions we consider in order to minimize $f_{\text{low-}z}$. All galaxies plotted here are single-line emitters with $\lambda_{\text{obs}} \leqslant 1.05$ μm. Galaxies that are undetected in the UVIS filter(s) are plotted as squares: either solid if both V_{606} and I_{814} imaging are available or open if we have only I_{814}. The selected LAE candidates are indicated by red squares. The 1α error bars are shown, and nondetections are plotted at the 1σ magnitude limits calculated for their fields. Typical error bars for the UVIS-detected galaxies are plotted in the lower right corner. There are three additional UVIS nondetections (black squares) that lie outside the selection region. We discuss these sources in Appendix B but do not consider them $z > 6$ LAE candidates due to their red IR colors.

3.2. Selection Criteria

A WISP single-line emitter is identified as a $z > 6$ LAE candidate if and only if it

1. has a single emission line at $\lambda_{\text{obs}} \leqslant 1.05$ μm;
2. is detected with a signal-to-noise (S/N) ratio in J_{110} of $(\text{S/N})_{J_{110}} \geqslant 5$;
3. has colors consistent with those of a $z \geqslant 6$ galaxy:

$$(I_{814} - J_{110}) \geqslant 0.5,$$
$$(J_{110} - H_{160}) \leqslant 0.5; \quad (2)$$

4. is undetected at the 1σ level in all available UVIS filters ("UVIS dropouts").

We derive the color selection criteria in Appendix A and identify it by the shaded region in Figure 1. These color criteria are comparable to those used in similar searches for $z \sim 6$–7 galaxies, such as Oesch et al. (2010), Schenker et al. (2013), and Bouwens et al. (2015), who employ color cuts of $(I - J) > 0.7 - 1$ and $(J - H) < 0.4 - 1$ in the same or similar filters as those used here.

We adopt the 1σ limiting magnitudes for all galaxies that are 1σ nondetections[15] and plot them in Figure 1 as limits. Each LAE candidate is then inspected by eye to confirm the emission lines are real and the galaxy is truly undetected in the UVIS filters.

[15] In order to confirm the detection or nondetection of each source, we measure the residual flux of the surrounding sky. We place the same-size circular apertures ($r = 0\farcs3 = 7.5$ pix) randomly on the sky around each source out to a radius of $5''$. A source that is fainter than $\geqslant$84% of these sky apertures is considered a 1σ nondetection in that filter.

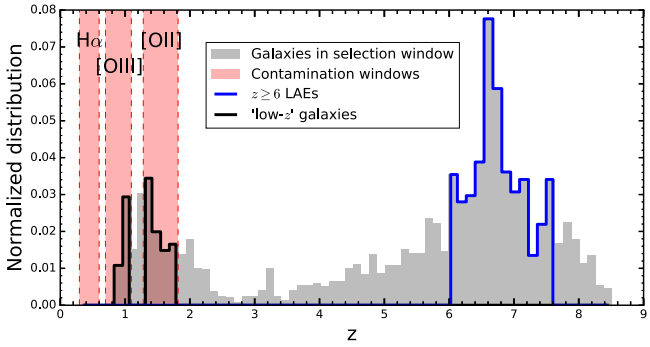

Figure 2. Characterization of the expected contamination in the LAE sample from the synthetic catalog derived in Appendix A. The redshift distribution of UVIS nondetections in the color selection window is shown in gray. The distribution of the high-z population we are targeting ($6.0 \lesssim z \lesssim 7.6$) is outlined in blue. The shaded red bands indicate redshift windows capable of contributing contaminants to the high-z sample, and the distributions of galaxies within these bands are outlined in black. These galaxies account for 29% ($f_{\text{low-}z}$) of the total selected sample (blue + black). WISP has the spectral coverage to detect multiple emission lines in the spectra of these "low-z" galaxies. As a result, only those with additional emission lines fainter than the WISP sensitivity would contaminate the LAE sample (~2%; see Section 4).

4. Contamination

High-redshift samples selected via the Lyman break technique can be highly contaminated by lower-redshift interlopers. If, for example, there is any overlap between the red and blue filters, as between I_{814} and J_{110}, the dropout color as a function of redshift can flatten into a "color plateau" (Stanway et al. 2008). Photometric uncertainty can scatter lower-redshift galaxies into the selection window while simultaneously scattering real high-redshift sources out. Additionally, Balmer break galaxies at $1.3 \lesssim z \lesssim 2.5$ can mimic the colors of $z \geqslant 6$ galaxies in filters chosen to bracket the Lyman break (e.g., Mobasher et al. 2005; Henry et al. 2009; Pirzkal et al. 2013).

We characterize the expected contaminants to the LAE sample in Figure 2. The gray histogram shows the redshift distribution of sources from our synthetic catalog that lie in the selection window and are nondetections in both V_{606} and I_{814}. These sources have redshifts in the range $0.7 \lesssim z \lesssim 8.5$ and include a large number of $z < 6$ galaxies.

However, as described in Section 3.1, we consider single-line emitters with lines in the range $0.85 \lesssim \lambda_{\text{obs}} \leqslant 1.05$ μm. We remind the reader that the red wavelength limit is chosen to minimize contamination, and the blue limit is determined by the rapid drop in the grism sensitivity. Given these wavelengths, we are probing Lyα at

$$6.00 \lesssim z_{\text{Ly}\alpha} \lesssim 7.63. \quad (3)$$

Galaxies in this redshift range are identified by the blue histograms in Figure 2. The wavelength selection also restricts contaminants to very narrow redshift ranges (identified as red-shaded regions in Figure 2):

1. Hα at $0.3 \lesssim z_{\text{H}\alpha} \lesssim 0.6$,
2. [O III] at $0.7 \lesssim z_{[\text{O III}]} \lesssim 1.1$, and
3. [O II] at $1.3 \lesssim z_{[\text{O II}]} \lesssim 1.8$.

The galaxies from these redshift regions are outlined in black, and the resulting fraction of lower-z sources that are selected alongside the $z > 6$ galaxies is $f_{\text{low-}z} = 0.29$. This fraction, however, is much higher than the contamination fraction we expect for the LAE sample, f_{contam}, which is limited to

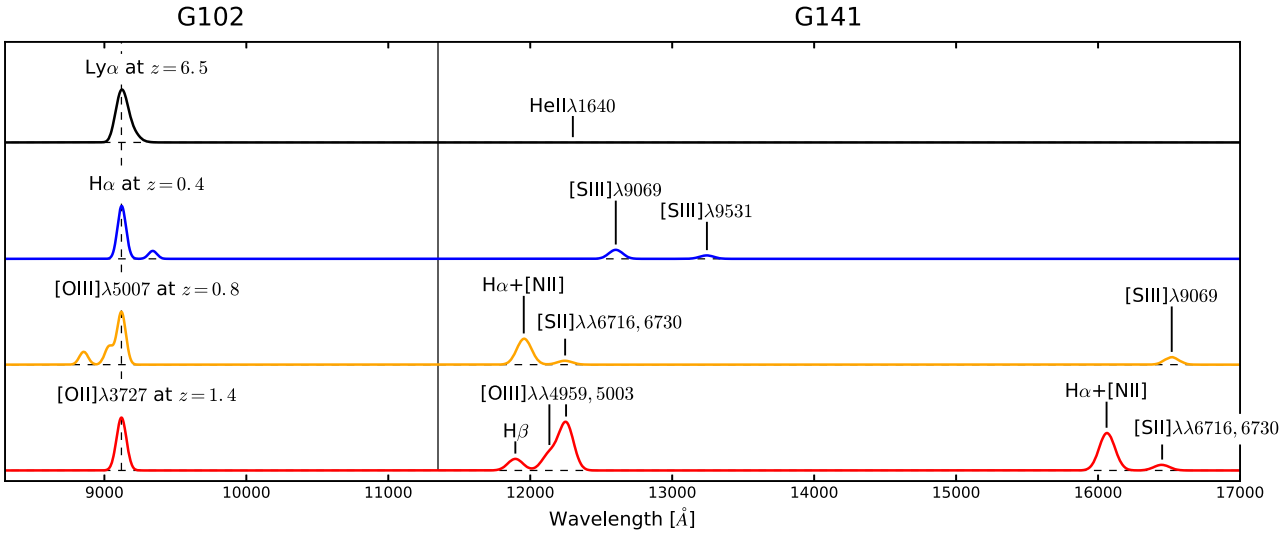

Figure 3. An illustrative example of how the full wavelength coverage of WISP can be used to rule out lower-z interlopers. We show here three possible misidentifications, where Hα at $z = 0.4$ (blue), [O III] at $z = 0.8$ (orange), and [O II] at $z = 1.4$ (red) are mistaken for Lyα at $z = 6.5$ (black). In each case, we expect to detect additional emission at longer wavelengths. We can therefore rule out all lower-z contaminants but those where the redder emission lines fall below the WISP sensitivity. The spectra plotted here have been convolved to match the resolutions of the G_{102} and G_{141} grisms.

lower-redshift galaxies with very specific emission line ratios (see Section 4.1). In what follows, we show that very few galaxies ($\lesssim$2%) in these redshift ranges could contaminate our results.

If the LAE candidates are lower-z contaminants, we would expect to detect additional emission lines in the G_{141} grism. For the purposes of illustration, we plot a simplified emission line spectrum in Figure 3 at four redshifts: $z = 6.5$ (black), 1.4 (red), 0.8 (orange), and 0.4 (blue). Because we select the LAE candidates from the sample of single-line emitters in the WISP catalog, no additional emission lines are detected in the spectra of these galaxies over the full wavelength coverage of the WISP survey. Therefore, if they are lower-redshift galaxies, the additional emission lines must fall below the sensitivity of the WISP spectra.[16] We discuss this possibility in the following section.

4.1. Emission Line Misidentification

In the case that the Lyα emission line has been misidentified, it would likely be either Hα, [O III], or [O II] from lower-z galaxies. It is difficult to rule out Hα emitters based on the candidates' spectra because there are few emission lines detected redward of Hα in WISP spectra. From our synthetic catalog, however, we find that all galaxies in the redshift range in which Hα can enter our sample are detected in the UVIS images (see Figure 2). Therefore, we conclude that contamination from Hα is negligible.

For the remaining likely contaminants, [O III] and [O II] emitters, we look to the full WISP emission line catalog for information on the expected line ratios of galaxies at $z \lesssim 2$. The [O III] doublet is blended at the resolution of the WFC3 grisms, so we use [O III] to refer to [O III] $\lambda\lambda$4959, 5007 in what follows. Similarly, Hα fluxes are not corrected for [N II]. Figure 4 shows the Hα/[O III] (left panel) and [O III]/[O II] (right panel) line ratios for sources in the WISP catalog. Here we consider all sources for which the bluer of the two emission lines lies in our wavelength selection range ($0.85 \lesssim \lambda_{\rm obs} \leqslant 1.05$ μm). For example, if an emission line at $\lambda_{\rm obs} = 0.9$ μm is [O III] instead of Lyα, then we would expect to detect Hα at $\lambda_{\rm obs} = 1.18$ μm. The shaded areas in Figure 4 show the approximate regions of lower limits in the case where Hα (left) or [O III] (right) are undetected in the WISP spectra. For both cases we adopt 2×10^{-17} erg s^{-1} cm^{-2} as the limiting line flux, which is the average line flux limit in the deep WISP fields.[17] The line ratios for the $z = 0.8$ and $z = 1.4$ spectra plotted in Figure 3 are indicated in Figure 4 by orange and red squares, respectively, and are meant as illustrative examples for reference only.

The median line flux ratios in the WISP catalog are Hα/[O III] ~ 1 and [O III]/[O II] ~ 2.5, consistent with previous results from both individual galaxies (Mehta et al. 2015) and stacked WISP spectra (Domínguez et al. 2013; Henry et al. 2013). If the LAE candidates are lower-z contaminants, their line ratios would have to be extreme: Hα/[O III] or [O III]/[O II] $\lesssim 0.2$ for fluxes of $\sim 1 \times 10^{-16}$ erg s^{-1} cm^{-2}. In other words, if the single detected emission line is actually [O III] ([O II]), then Hα ([O III]) must be a factor of $\gtrsim$5 fainter to fall below our sensitivity.

As can be seen from the right panel of Figure 4, [O II] emitters will not contaminate the LAE sample. At line fluxes of $f = 1 \times 10^{-16}$ erg s^{-1} cm^{-2}, virtually no galaxies have [O III]/[O II] < 0.2. Because [O III] is so much stronger than [O II], we are guaranteed not to mistake [O II] for Lyα. On the other hand, 2% of galaxies with $7 \times 10^{-17} \leqslant f_{\rm [O\,III]} \leqslant 2 \times 10^{-16}$ erg s^{-1} cm^{-2} have Hα/[O III] < 0.25. Hence, contamination from [O III] emitters is very rare but still a possibility.

There is always the possibility that hot pixels, cosmic rays, and other artifacts are masquerading as emission lines, although we expect only an $\sim$8.5% contamination rate due to false

[16] It is also possible that a second emission line could fall on the overlapping edge of the two grisms and be lost due to the drop in sensitivities. Such galaxies would be mistakenly identified as single-line emitters. This would only occur, however, for a small subset of emission lines in the range $1.13 \lesssim \lambda_{\rm obs} \lesssim 1.15$ μm and does not affect the LAE candidates. If the candidates are lower-z galaxies, the additional emission lines such as [O III] and Hα would not fall in the affected wavelength range.

[17] Emission lines with fluxes below this value are either in the deepest fields or are detected at lower significance than the rest of the catalog. If there are multiple emission lines in the spectra, the secondary lines are measured even if they are at lower S/N.

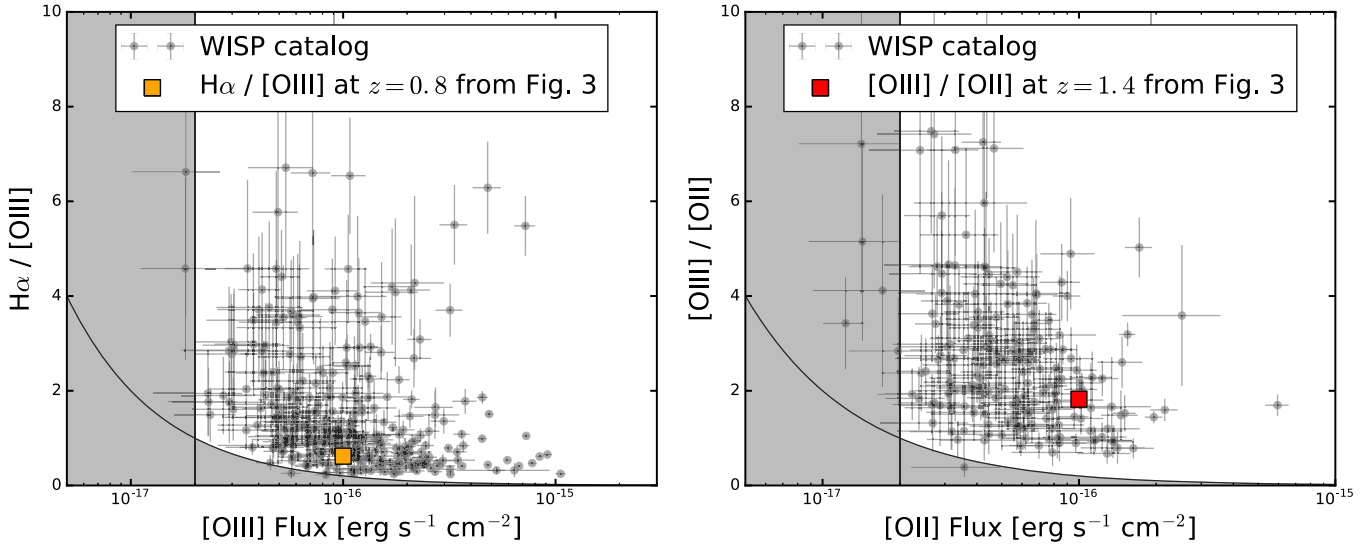

Figure 4. The line ratios for all sources in the WISP catalog for which the bluer of the two emission lines lies in our wavelength selection range ($0.85 \lesssim \lambda_{\rm obs} \leqslant 1.05\ \mu$m). Left: H$\alpha$/[O III] as a function of [O III] flux. Right: [O III]/[O II] as a function of [O II] flux. The shaded areas show the regions where one of the emission lines is below the detection limit of the WISP spectra, assuming 2×10^{-17} erg s^{-1} cm^{-2} as the limiting line flux. For reference, the orange and red squares show the line ratios for the $z = 0.8$ (orange) and $z = 1.4$ (red) spectra in Figure 3.

emission lines (Colbert et al. 2013). Due to the different dispersion solutions, the spectra do not fall on exactly the same pixels in G_{102} and G_{141}. By comparing the full dispersed images in each grism, we performed a check for hot pixels, detector artifacts, and persistence that could have been incorrectly identified as emission lines. We also inspected each individual grism exposure to ensure that we are not detecting cosmic rays. Finally, we have checked that the emission lines in our sample are not zeroth orders from nearby objects. All galaxies in our sample lie sufficiently far from the right edge of the detector, so zero-order images are easily identified for their spectra.

Considering contamination from both lower-z and false emission lines, we expect the contamination fraction in the LAE sample to be no higher than $f_{\rm contam} \sim 2\%$–8%.

5. Results

5.1. LAEs at $z > 6$

We find two robust candidates according to the selection criteria described in Section 3: *WISP368* at $z = 6.38$ and *WISP302* at $z = 6.44$. Table 2 summarizes the spectroscopic and photometric properties. For both sources, a large fraction of the flux density in J_{110} is due to the emission line, and we include this fraction, $f^{\rm neb}_{J110}/f^{\rm total}_{J110}$, in Table 2. We calculate the rest-frame EW of Lyα using the H_{160} magnitudes for the continuum measurement, as the H_{160} magnitudes are not contaminated by Lyα emission. In the case of *WISP368*, we adopt the 3σ H_{160} magnitude limit. We also present the UV absolute magnitudes calculated at rest-frame wavelengths of 1500 Å and 2000 Å, corresponding to J_{110} and H_{160}, respectively. The parameter M_{1500} is calculated using the J_{110} magnitude corrected for the emission line flux. Still, M_{1500} is uncertain, so we do not calculate the UV slope β. Finally, we measure 3σ upper limits for He II λ1640 and C III] λ1909 fluxes.

We present images of each candidate in Figure 5. The stamps are 3″ on a side and are each smoothed with a Gaussian kernel with $\sigma = 1$ pixel. The candidates have dropped out of the UVIS filters: V_{606} and I_{814} for *WISP302* and I_{814} for *WISP368*.

Figure 6 shows the one- and two-dimensional G_{102} and G_{141} spectra for each candidate. The Lyα emission lines are circled in white. Additional "emission features," identified in black in Figure 6, are present in the dispersed images of both objects. After careful examination of the images, we conclude that these features belong to nearby sources. The wavelengths of He II λ1640 and C III] λ1909 are also labeled.

We use a Monte Carlo process to measure the line fluxes: we fit the line with a Gaussian, allow the flux at each wavelength step to vary within the uncertainties, and refit. The flux uncertainties in Table 2 are the 1σ dispersion in the distribution of measured fluxes.

5.2. What Are the Redder UVIS Dropouts?

There are three additional sources (black squares in Figure 1) that are too red to fall in our selection window yet meet all other criteria. As single-line emitters that drop out of the UVIS filters, these sources are worth further consideration. These three galaxies are small and compact and lie in the region of color space that contains a higher fraction of the dusty, red, lower-z galaxies in our synthetic library. Such galaxies may belong to a population of galaxies at $z \sim 1.5$–1.8 that are either very dusty or have strong 4000 Å breaks, causing them to mimic the broadband colors of the Lyman break. The emission line is most likely [O II]. According to Maiolino et al. (2008), the observed limit of [O III]/[O II] ([O III]/[O II] $\lesssim 0.2$–0.25) would imply high metallicities at these redshifts. Understanding the nature of these sources is very important but beyond the scope of this paper. We do not consider these three sources in our analysis and instead present their spectra and direct image stamps in Appendix B.

5.3. Calculation of the Number Density

Given the two LAEs presented above, we calculate the number density as

$$n_{\rm LAE} = \sum_i C_i \frac{1}{V_i}, \quad (4)$$

Table 2
Lyman Alpha Emitters

ID	R.A. (J2000)	Decl. (J2000)	$z_{Ly\alpha}$	$f_{Ly\alpha}$ (10^{-17} erg s^{-1} cm^{-2})	EW$_0$ (Å)	$L_{Ly\alpha}$ (10^{43} erg s^{-1})	f_{HeII}[a] (10^{-17} erg s^{-1} cm^{-2})	$f_{C\,III]}$[a] (10^{-17} erg s^{-1} cm^{-2})
WISP302	02:44:54.72	−30:02:23.3	6.44	9.9 ± 5.8	798 ± 531	4.67	<6.0	<4.3
WISP368	23:22:32.26	−34:51:03.7	6.38	10.2 ± 3.9	<1172	4.71	<3.9	<2.8
ID	V_{606}[b] (mag)	I_{814}[b] (mag)	J_{110}[b] (mag)	$f^{neb}_{J110}/f^{total}_{J110}$	H_{160}[b] (mag)	M_{1500}[c] (mag)	M_{2000} (mag)	
WISP302	>27.86	>27.49	26.0 ± 0.11	0.67	26.1 ± 0.35	−19.6	−20.7	
WISP368	···	>27.78	26.3 ± 0.20	0.96	>27.67	−17.0	>−19.1	

Notes.
[a] Flux limits are 3σ.
[b] Total magnitudes as measured by *Source Extractor*'s AUTO elliptical apertures.
[c] M_{1500} is calculated using the J_{110} magnitude corrected for the emission line flux.

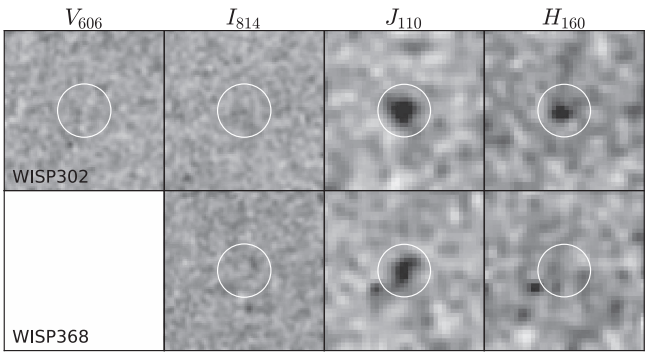

Figure 5. Direct image postage stamps of the LAEs. Columns show, from left to right, V_{606}, I_{814}, J_{110}, and H_{160}. All stamps are 3″ on a side. The UVIS stamps have a pixel scale of 0.″04/pix, and the IR stamps have been redrizzled here onto a pixel scale of 0.″08/pix. All stamps are smoothed with a Gaussian kernel with $\sigma = 1$ pixel ($\sigma = 0.''04$ and 0.″08 in the UVIS and IR, respectively). The white circles are 0.″5 in radius.

where C_i is an emission-line-dependent completeness correction, and V_i is the volume within which the emission line could be detected. The dominant sources of incompleteness in the WISP survey are (1) confusion from nearby objects and partially or fully overlapping spectra, and (2) the failure of the line-finding process to identify emission lines. Colbert et al. (2013) simulate the full emission line identification process and derive completeness corrections that depend on emission line EW and line flux S/N. We do not detect continua in the LAE spectra, so we use the completeness corrections appropriate for the highest-EW lines in the WISP catalog.

The WISP fields reach a range of depths. In determining V_i we use a modified version of the $V_{\rm MAX}$ method (Felten 1977) that depends on the G_{102} sensitivity limit reached in each WISP field. The maximum volume within which a galaxy with the given absolute Lyα luminosity could be detected is

$$V_{\rm MAX}({\rm LAE}) = \sum_{i=1}^{N_{\rm fields}=48} \Omega_i \int_{z_{L,i}}^{z_{U,i}} \frac{dV}{dz} dz. \quad (5)$$

Here, Ω_i is the effective area of one WISP field (3.3 arcmin^2); z_L is the lower redshift at which the galaxy's Lyα luminosity would fall below the G102 grism sensitivity, which cuts off steeply at the blue end; and z_U is the minimum of (1) the redshift at which the galaxy's line flux would fall below the sensitivity on the red side, and (2) the upper redshift limit set by our selection criteria, $z = 7.63$. The Lyα LF, however, is expected to evolve rapidly above $z = 7$. For the purposes of comparing our number counts with those of other studies at $z \sim 6.5$, we limit this maximum redshift to $z = 7$. We present an upper limit for the volume at $7.0 \leqslant z \leqslant 7.63$ in Section 6.2.

The integration limits in Equation (5) are calculated for each of the 48 fields because the depth is not uniform across all fields. This corresponds to different redshift limits, z_U and z_L, and therefore different volumes probed in each field. Smaller effective volumes are probed in the shallower fields. In some cases, the emission line may not be detectable in a shallow field at any of the relevant redshifts.

Figure 7 shows a schematic representation of this process. As an example, two curves are plotted in gray showing the flux of a Lyα emission line as it would be observed if the galaxy were placed at a range of redshifts. The curves show the fluxes corresponding to $L_{{\rm Ly}\alpha} = 2 \times 10^{43}$ erg s^{-1} (dashed) and $L_{{\rm Ly}\alpha} = 2.5 \times 10^{43}$ erg s^{-1} (solid). In the first case, the emission line is too faint to be detected in this field at any redshift. In the second case, the redshifts at which the flux would drop below the grism sensitivity are marked by solid blue lines. The redshift limits in this field would be $z_L = 6.31$ and $z_U = 7.00$, where we fix z_U to calculate the effective volume at $z \sim 6.5$. For the volume calculation at $z \geqslant 7$, $z_L = 7$ and $z_U = 7.63$. Figure 8 shows the total effective volume calculated in all 48 WISP fields as a function of line luminosity. The total volume probed in WISP fields at the luminosity of the LAEs is 5.8×10^5 Mpc^3 at $6 \lesssim z \leqslant 7$. For comparison, the volumes covered by the $z \simeq 6.5$ ground-based narrowband surveys we consider in this paper are 1.5×10^6 Mpc^3 (Hu et al. 2010), 8×10^5 Mpc^3 (Ouchi et al. 2010), 2.17×10^5 Mpc^3 (Kashikawa et al. 2011), and 42.6×10^5 Mpc^3 (Matthee et al. 2015). Extending the redshift range out to $z = 7.63$ would add another $\sim 2.2 \times 10^5$ Mpc^3 to the WISP volume.

We compare the number density of $z \sim 6.5$ LAEs in the WISP survey to measurements of the Lyα cumulative LF in Figure 9. The completeness-corrected number density calculated according to Equation (5) is plotted as the solid red circle. The observed number density—calculated without the completeness correction—is plotted as the smaller, open red circle. The uncertainty on n is plotted as the Poissonian error for small-number statistics and is taken from Gehrels (1986). The uncertainty on $\log(L_{{\rm Ly}\alpha})$ is dominated by the large flux uncertainty of *WISP302*.

The WISP LAEs are among the brightest discovered at these redshifts. Recently, a handful of comparably bright LAEs have been detected and spectroscopically confirmed in the COSMOS field. The two brightest, CR7 (Matthee et al. 2015; Sobral et al. 2015) and COLA1 (Hu et al. 2016), are plotted here in blue. The number density for CR7 is calculated using the full volume that Matthee et al. (2015) probe in the UDS, COSMOS, and SA22 fields, 42.6×10^5 Mpc^3. Hu et al. (2016) cover an additional ~ 2 deg^2 in COSMOS, which we roughly convert to a volume using the width of the narrowband filter *NB*921 the authors used to discover the bright LAEs. COLA1 was discovered in this additional area, which probed a combined volume of $\sim 58.6 \times 10^5$ Mpc^3. In each luminosity bin, the open blue circles show the observed number densities. The closed blue circles are the number densities corrected for the shape of the *NB*921 filter profile using the luminosity-dependent correction factors presented in Matthee et al. (2015).

We plot the $z \sim 6.5$ cumulative LFs of Hu et al. (2010), Ouchi et al. (2010), Kashikawa et al. (2011), and Matthee et al. (2015) in Figure 9 and discuss this comparison in Section 6.1.

5.4. Extended Lyα Emission

LAEs are expected to have extended Lyα emission. Lyα photons created in star-forming regions are resonantly scattered outward, creating large diffuse halos of extended Lyα emission (Zheng et al. 2010). At $z \geqslant 6$, where the surrounding IGM is partially neutral, the Lyα halo could extend as far as 1 Mpc from the galaxy (Zheng et al. 2011). Evidence for extended Lyα halos has been detected around galaxies at $z \sim 0$ (Hayes et al. 2014), $z \sim 2$–3 (e.g., Steidel et al. 2011; Matsuda et al. 2012), and $z = 3$–6 (Wisotzki et al. 2016). At $z \geqslant 6$, these analyses are incredibly difficult to perform on individual galaxies, and

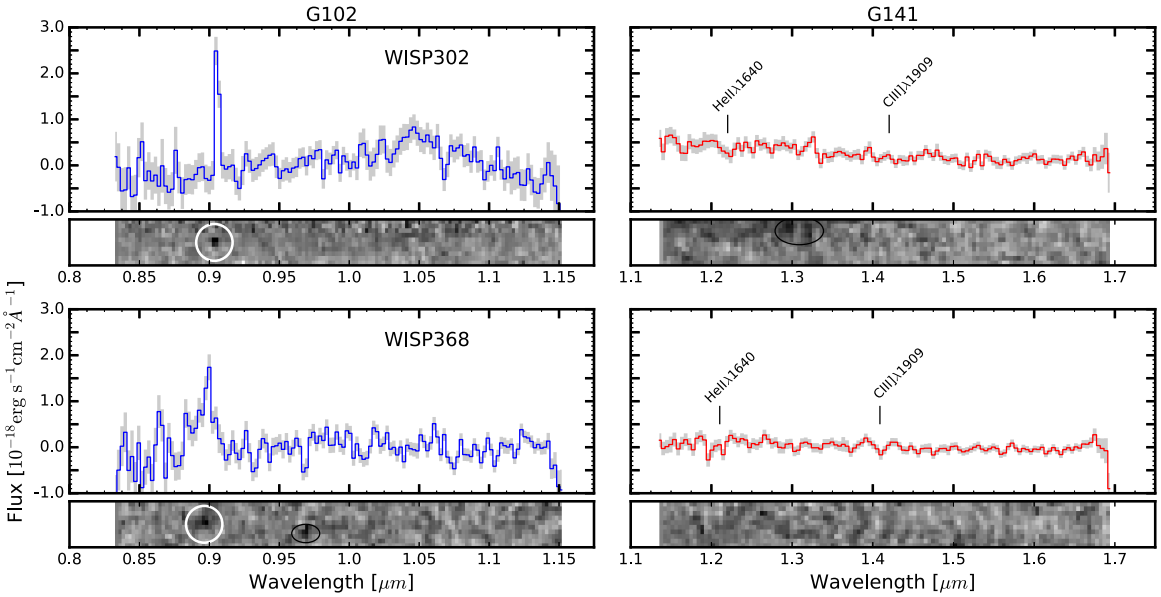

Figure 6. The one- and two-dimensional spectra of the LAE candidates in G_{102} (left column) and G_{141} (right). In the one-dimensional spectra, the 1σ errors are plotted in gray. The grism spectral stamps have been smoothed by 0.5 pixels. The Lyα emission lines are circled in white, and nearby "emission features" are identified in black.

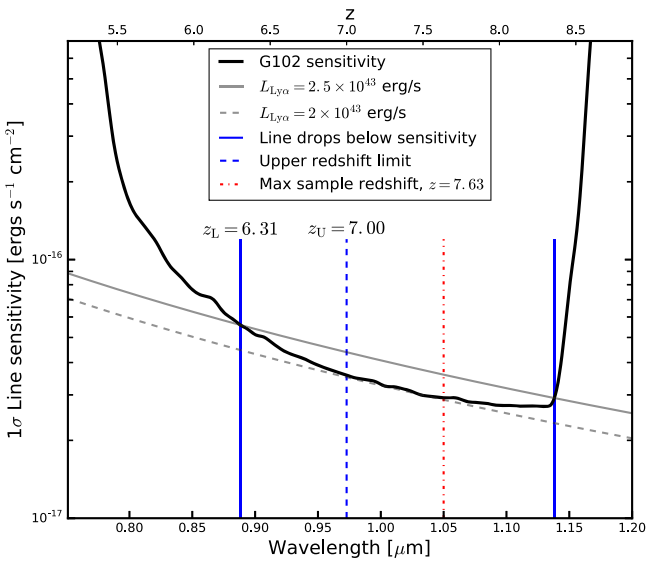

Figure 7. Schematic representation of the modified V_{MAX} method used to calculate the volume within which an emission line of a given luminosity is detectable by the WISP survey. The black curve is the G102 sensitivity limit calculated for one of the fields. The solid gray curve shows the observed flux of a Lyα emission line with $L_{Ly\alpha} = 2.5 \times 10^{43}$ erg/s at a range of redshifts. The redshifts at which the emission line drops below the sensitivity curve are indicated by blue solid lines. In calculating the volume at $z \sim 6.5$, we set $z_U = 7$ (blue dashed line), while the maximum redshift limit of our sample ($z = 7.63$) is indicated by a red dash-dotted line. The dashed gray curve shows the observed Lyα flux for $L_{Ly\alpha} = 2 \times 10^{43}$ erg s^{-1} which would not be detected in this field.

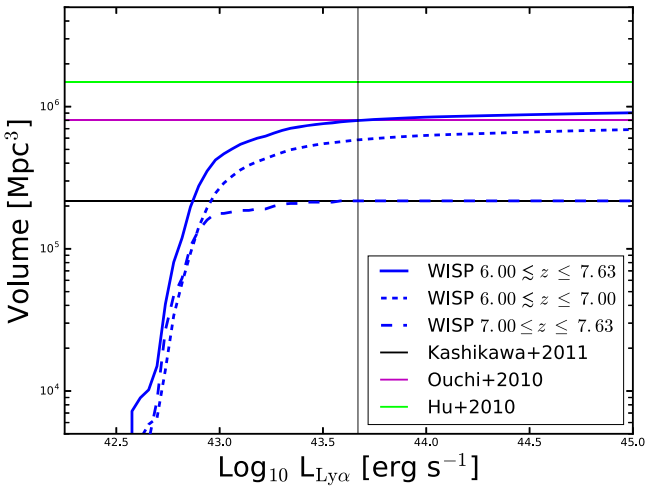

Figure 8. The total effective volume reached in all 48 WISP fields as a function of luminosity. The solid curve shows the volume probed over the full redshift range, $6.00 \lesssim z \leq 7.63$. The lower redshift limit comes from the drop in sensitivity of the G_{102} grism at the blue end, while the upper redshift limit corresponds to our wavelength criterion $\lambda_{obs,max} = 1.05\ \mu$m. The dashed curve shows the volume probed at $6 \lesssim z \leq 7$, which is used to calculate the number density of WISP LAEs in Figure 9. The dotted curve shows that the volume probed at $7.00 \leq z \leq 7.63$, which is used to place a limit on the number of WISP LAEs at $z > 7$ (see Figure 12).

narrowband images are almost always stacked (Momose et al. 2014).

In the two-dimensional WISP spectra extracted from the full grism images, spatial information is preserved along the cross-dispersion axis. We can therefore measure the spatial extent of Lyα emission around the LAEs in our sample. We create stamps of the 2D spectra around the emission line of each LAE. There are no continua detected in the spectra, but to be sure we fit the background row by row on either side of the emission line and subtract it out of the spectral stamp.

In each stamp, four columns of pixels (~100 Å) centered on the emission line are collapsed along the wavelength direction. This results in a one-dimensional profile of the Lyα emission along the spatial axis, as shown in blue in Figure 10. In the same way we collapse the continuum image of the galaxy in J_{110} and H_{160} along the same axis and plot these profiles as solid and dashed lines, respectively. As *WISP368* is not detected in H_{160}, we plot only the J_{110} profile for this LAE. All profiles are normalized to the peak values for easy comparison of the profile shapes.

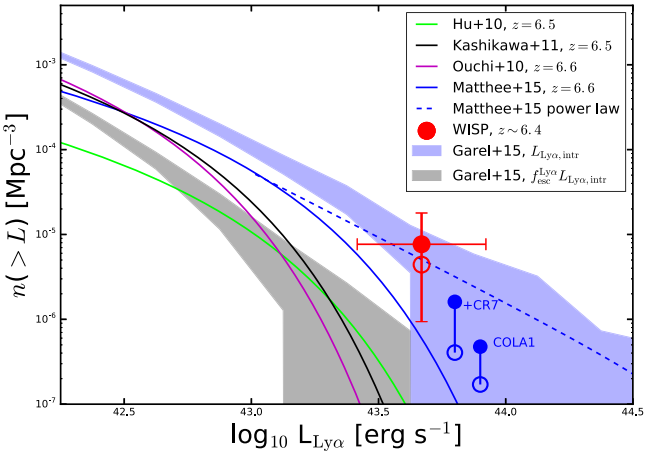

Figure 9. The number density of WISP LAEs at $z \sim 6.5$. The WISP number densities are plotted in red, both with (solid circle) and without (open circle) completeness corrections. The observed (open blue circles) and corrected (solid blue circles) number densities calculated using the brightest LAEs discovered in COSMOS, CR7 and COLA1, are shown for comparison. The cumulative LFs of Hu et al. (2010), Kashikawa et al. (2011), Ouchi et al. (2010), and Matthee et al. (2015) are plotted as solid lines. The dashed blue line shows the integration of the power-law fit to the bright end of the LF from Matthee et al. (2015). The shaded regions show the 1σ dispersions of the cumulative LF calculated from 100 realizations of the mock light cones from Garel et al. (2015). The light blue and gray regions show, respectively, the results using the intrinsic Lyα emission and that which is able to escape.

We measure Lyα and continuum emission that are both equally compact, with FWHM of $\sim$0.″4. This corresponds to $\sim$2.2 kpc at these redshifts. Unfortunately, our measurements are limited by the depth of the WISP spectra. Extended Lyα emission may be present below our surface brightness limit. We discuss this possibility in Section 6.3.

6. Discussion

6.1. The Number Density of $z \sim 6.5$ LAEs

The WISP survey is probing the most luminous LAEs at $z \geqslant 6$, a population that can provide important information about the state of the IGM at these redshifts. It is expected that the observed number density of LAEs decreases as the volume-averaged neutral hydrogen fraction of the IGM, x_{HI}, increases. Upon encountering neutral hydrogen, photons at the Lyα resonance are scattered out of the line of sight. Drops in the observed number densities of LAEs from $z \sim 5.5$ to 7 (e.g., Hu et al. 2010; Ouchi et al. 2010; Kashikawa et al. 2011) are often interpreted as evidence of an increasingly neutral IGM and indirect measurements of the end of reionization.

Lyα photons can escape from the surroundings of a galaxy during the epoch of reionization if the galaxy lies in an ionized bubble large enough to allow the photons to redshift out of resonance before encountering the neutral IGM at the edge of the H II region. We can expect, then, to preferentially observe the most luminous LAEs—those capable of ionizing the largest bubbles—at earlier times during reionization (e.g., Matthee et al. 2015; Hu et al. 2016). As x_{HI} increases with redshift, Lyα emission from fainter galaxies—those that cannot create bubbles out to sufficiently large radii—will be increasingly suppressed. The more luminous galaxies are already surrounded by ionized media and so are less affected.

Recent studies have indicated that the observed number density of bright LAEs is relatively unchanged from $z \sim 6.5$ to $z = 5.7$ compared with that of the fainter LAEs (Matthee et al. 2015; Santos et al. 2016). This effect can be seen as a flattening of the Lyα LF at the bright end. Matthee et al. (2015) find that the bright end of the $z = 6.6$ Lyα LF is best fit by a power law, indicating that there are more bright LAEs than expected for a Schechter-like LF. In a continuation of the same survey, Santos et al. (2016) find that while there is a drop in the number densities of faint LAEs from $z = 5.7$ to $z = 6.6$, there is almost no evolution at the bright end. This result could indicate that the brightest galaxies already reside in ionized bubbles by $z \sim 6.5$. Remarkably, our results are consistent with the measurements of Matthee et al. (2015) and Santos et al. (2016).

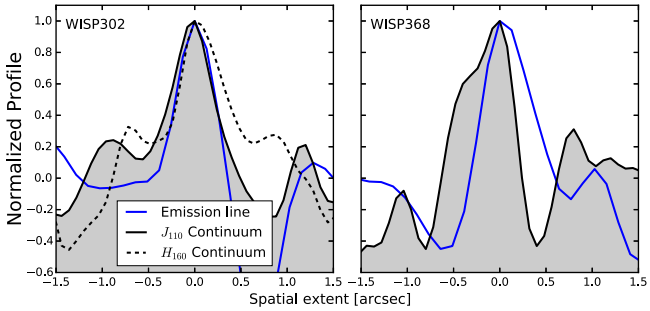

Figure 10. The spatial profile of emission from the LAEs. The Lyα profile is measured in the two-dimensional spectral stamps and is plotted in blue. The solid and dashed black curves show the extent of the continuum emission measured in the J_{110} and H_{160} image stamps, respectively. Both the Lyα and continuum emission are compact. The Lyα spatial profiles have FWHM $= 0.''38$ (left, *WISP302*) and $0.''46$ (right, *WISP368*). There is a slight offset ($\sim 0.''3$ measured at half-maximum) between the Lyα and continuum profiles of *WISP368*.

Other studies show the opposite effect. Kashikawa et al. (2011) find a deficit of bright LAEs at $z = 6.5$ as compared with $z = 5.7$. Additionally, at $z = 6.5$, the number densities of bright LAEs measured by Hu et al. (2010), Ouchi et al. (2010), and Kashikawa et al. (2011) are all far below those of the WISP fields (see Figure 9). For example, Kashikawa et al. (2011) find only one LAE with $L_{\mathrm{Ly}\alpha} > 10^{43}$ erg s^{-1}. This result, however, may be heavily influenced by cosmic variance. While Kashikawa et al. (2011) survey a much larger area ($\sim$900 arcmin^2) than that presented here ($\sim$160 arcmin^2), they cover only a single pointing in a narrow redshift range. Meanwhile, the 48 pure-parallel WISP fields presented in this paper are completely uncorrelated. We estimate that the cosmic variance in the WISP sample is $<$1% (Trenti & Stiavelli 2008), compared with the $\sim$30% of Kashikawa et al. (2011). The 24%–34% decrease Kashikawa et al. (2011) find in the number density of LAEs from $z = 5.7$ to $z = 6.5$ may be due in part to cosmic variance. However, at $\log(L_{\mathrm{Ly}\alpha}) \sim 43.5$, Matthee et al. (2015) observe a number density that is $\sim$100 times higher than that of Kashikawa et al. (2011), a difference that cannot be explained by cosmic variance alone. Enhanced clustering of LAEs introduced by reionization (e.g., McQuinn et al. 2007) could explain some of this observed difference.

We note that the surveys presented in Figure 9 have different EW limits, a situation that can affect the measured LFs (see, for example, the SED models presented by Konno et al. 2016). However, Ouchi et al. (2008) show through Monte Carlo simulations that when they consider all LAEs down to a rest-frame EW of EW$_0 = 0$ Å, the normalization of the Schechter LF, ϕ^*, increases by $\lesssim$10% compared with that for EW limits of EW$_0 \sim$ 30–60 Å. This exercise indicates that the $\sim$5–10 Å difference between the EW limits of the WISP Survey and those of, for example, Ouchi et al. (2010) and Kashikawa et al. (2011) will have at most a minor effect on the number density

of LAEs we observe. Additionally, given their fluxes and EWs, the WISP LAEs and those discovered by Matthee et al. (2015) at the bright end would have been easily detected in the narrowband surveys of Ouchi et al. (2010) and Kashikawa et al. (2011).

In Figures 9 and 12, we also compare our results to predictions from mock light cones based on the model of Garel et al. (2015) and adapted for the area and redshift range covered by the WISP fields. Garel et al. (2015) combine the GALICS semianalytic model with numerical simulations of Lyα radiation transfer through spherical, expanding shells of neutral gas and dust (Verhamme et al. 2006) to predict the emission of Lyα photons in high-redshift galaxies and their transfer in galactic outflows, ignoring the effect of IGM attenuation. GALICS describes the formation and evolution of galaxies within dark-matter halos extracted from a large cosmological simulation box ($L_{\rm box} = 100\,h^{-1}$ comoving Mpc). For each model galaxy, Garel et al. (2015) use scaling relations to connect the expansion velocity, column density, and dust opacity of the shell to the galaxy properties output by GALICS (see Garel et al. 2012 for more details). The Lyα line profiles and escape fractions are then estimated using the library of Lyα transfer models in shells presented in Schaerer et al. (2011).

The shaded regions in Figure 9 are the 1σ dispersion of the LF measured over 100 realizations of the mock light cones. The gray region, labeled $f_{\rm esc}^{\rm Ly\alpha}\,L_{\rm Ly\alpha,intr}$, shows the LF dispersion for mock light cones in which $f_{\rm esc}^{\rm Ly\alpha}$ is calculated as described above. We see that this model is in better agreement with the data of Hu et al. (2010), Ouchi et al. (2010), and Kashikawa et al. (2011), but it cannot reproduce the high number density of bright LAEs ($\log(L_{\rm Ly\alpha}) \gtrsim 43.5$) found in the WISP survey or by Matthee et al. (2015).

We see from Figure 9 that the dispersion of the LFs estimated from the mock light cones is significant at the bright end, which provides hints to the cosmic variance expected in our survey. However, the 1σ dispersion from the mock light cones cannot be reconciled with our data point even within the error bars, so it seems unlikely that field-to-field variation is responsible for the difference between our LF measurement and the LF estimated from the mock light cones or from the other surveys. Nevertheless, we note that cosmic variance is underestimated in the mock light cones of Garel et al. (2015) because of the finite volume of the simulation box they use, which misses the fluctuations on the very large scales.

Another interpretation of the difference between our measurements and the predictions from Garel et al. (2015) could arise from the fact that they do not account for the growth of the HII bubbles during the epoch of reionization when dealing with the Lyα transfer. Instead, for all model galaxies, Lyα photons need to travel through outflows of neutral gas and dust (as described above), which unavoidably reduce their observed luminosities. Interestingly, we find that our observed number density lies close to the mean LF of the Garel et al. (2015) models in which $f_{\rm esc}^{\rm Ly\alpha} = 1$ (the blue region, labeled $L_{\rm Ly\alpha,intr}$, in Figure 9). This might suggest that most Lyα photons can easily escape the bright WISP LAEs and that there is very little neutral hydrogen in their surrounding medium (see also Section 6.4).

The observed number density of the WISP LAEs is consistent with the density of the brightest LAEs detected to date at similar redshifts, CR7 and COLA1. The WISP number density is also consistent with that of model galaxies in a completely ionized IGM with $f_{\rm esc}^{\rm Ly\alpha} = 1$. We expect the WISP LAEs, like CR7 and COLA1, to reside in highly ionized bubbles. Such bubbles would enhance the field-to-field variations in the observed number counts of LAEs and may also partially explain the differences at the bright end between the LFs in Figure 9. We discuss these bubbles in Section 6.4.

If the ionized bubbles are large enough that emission blueward of the Lyα line center is not suppressed by the damping wings of the neutral IGM, we may expect the WISP LAE Lyα line profiles to have blue wings. Line profiles with both blue and red emission peaks are predicted for galaxies with low neutral hydrogen column densities (e.g., Verhamme et al. 2015). Double-peaked emission is common among "green pea" galaxies (Henry et al. 2015) and has been tentatively detected in the spectra of COLA1 (Hu et al. 2016). The detection of blue wings is beyond the resolution of WISP spectra and is one goal of planned follow-up observations.

As Konno et al. (2016) point out, at $z = 2.2$ all LAEs with $\log(L_{\rm Ly\alpha}) \gtrsim 43.4$ may be active galactic nuclei (AGNs). High-ionization emission lines such as C IV λ1549, He II λ1640, and C III λ1909 can be useful in identifying AGNs. However, these strong UV nebular emission lines may also indicate galaxies with young, metal-poor stellar populations and large ionization parameters (Panagia 2005; Stark et al. 2014, 2015, 2016). At the redshifts of the WISP LAEs, C IV λ1549 falls on the overlap region between G_{102} and G_{141}, where the sensitivity in the WISP spectra decreases significantly. We instead measure upper limits for He II λ1640 and C III] λ1909 fluxes (see Table 2). The limits we measure on the line ratios with respect to Lyα are too uncertain to allow us to determine the dominant source of photoionization, and we cannot distinguish between AGNs, metal-poor galaxies, and normal star-forming galaxies (Schaerer 2003; Stark et al. 2014). The emission lines we detect are unresolved, and therefore the FWHM is less than $\sim$1500 km s^{-1}. Although we can rule out broad-line AGNs, this limit does not allow us to distinguish between narrow-line AGNs and star-forming galaxies. We also notice that the Lyα rest-frame EW for the WISP LAEs is many times larger than what Konno et al. (2016) observe for AGNs of similar UV magnitudes. Finally, neither Sobral et al. (2015) nor Hu et al. (2016) find strong evidence of AGN emission in the CR7 and COLA1 spectra, although the possibility of an AGN contribution remains. We cannot draw specific conclusions about the physical characteristics of the LAEs from the present WISP data.

6.2. Evolution to $z \gtrsim 7$

Moving to higher redshifts, Konno et al. (2014) find a deficit at all luminosities at $z = 7.3$ compared to that at $z = 6.6$. This evolution of the Lyα LF may be the result of an increasing fraction of neutral hydrogen in the IGM during reionization. The authors also suggest that it could be due to the selective absorption of Lyα photons by neutral clumps in otherwise ionized bubbles. On the other hand, there have been several bright LAEs spectroscopically confirmed at $z \geqslant 7$ (e.g., Iye et al. 2006; Vanzella et al. 2011; Shibuya et al. 2012). Roberts-Borsani et al. (2016) recently discovered four galaxies at $z \sim 7$–9, all of which are emitting Lyα (Stark et al. 2016). With fluxes $f_{\rm Ly\alpha} \sim (0.7\text{–}2.5) \times 10^{-17}$ erg s^{-1} cm^{-2}, these $z > 7$ galaxies are all fainter than or on par with our detection limits.

We find no LAEs in the redshift range $7.0 < z < 7.63$ in the volume covered by the WISP fields, 2.17×10^5 Mpc^3. Assuming the Lyα LF does not evolve from $z = 6.5$ to

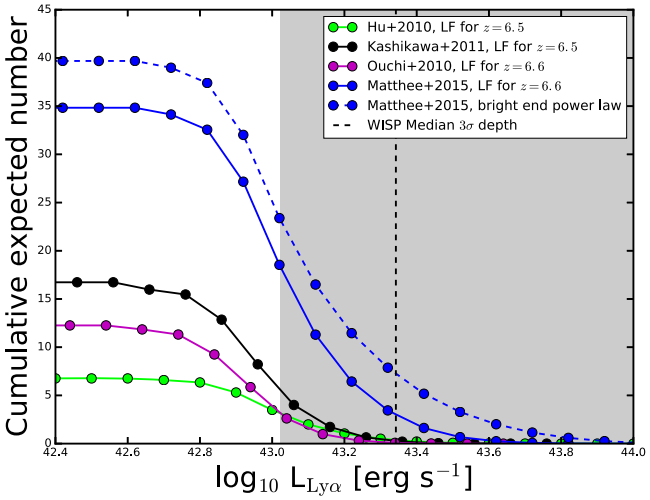

Figure 11. Expected number counts of LAEs at $z > 7$ assuming no evolution in the Lyα LF from $z \sim 6.5$. The shaded region indicates the range of 3σ depths in the WISP fields. The median 3σ depth is indicated by the vertical dashed line. Based on the four LFs from Figure 9, we would expect to detect between zero and three LAEs in the volume probed by the WISP survey at $7 \leqslant z \leqslant 7.63$. We can rule out evolution in the Lyα LF of Matthee et al. (2015), but we are unable to make a similar conclusion about the other three LFs.

$z = 7$, how many would we expect to observe? We calculate the expected number of LAEs at $7.00 \leqslant z \leqslant 7.63$ given the four $z \sim 6.5$ LFs in Figure 9 and the volumes probed by the 48 WISP fields in this redshift range. In Equation (5), we limit the redshift range so that $z_{L,i} \geqslant 7$ and $z_{U,i} \leqslant 7.63$, covering a volume of 2.17×10^5 Mpc^3. The results are plotted in Figure 11. The shaded region shows the luminosity range to which the WISP fields are sensitive. The edge of the region is plotted at the 3σ flux limit of the deepest field.

At the median 3σ depth of the WISP fields (dashed black line), we would expect to detect 3.4 LAEs at $7 \leqslant z \leqslant 7.63$ based on the Matthee et al. (2015) Schechter function LF (blue solid line). Given our nondetection at $z \geqslant 7$, we find that the probability that this $z = 6.6$ LF also applies at $z \geqslant 7$ is 3.3%. If we consider the authors' power-law fit to the bright end (dashed blue line), the expected number of $z \geqslant 7$ LAEs increases to 7.9, and the probability decreases to 0.037%. If either LF from Matthee et al. (2015) is representative at $z \sim 6.5$, we detect evolution in the Lyα LF from $z \sim 6.5$ to $z > 7$. However, given the LFs of Ouchi et al. (2010), Hu et al. (2010), and Kashikawa et al. (2011), we would expect to detect only 0.1–0.5 $z \geqslant 7$ LAEs. Our observations are inconclusive if these three LFs are more indicative of galaxy number densities at $z \sim 6.5$.

We next use the volume probed at $7 \leqslant z \leqslant 7.63$ to place a limit on the observable yet undetected number density of LAEs over this redshift range. This limit is shown as a red arrow in Figure 12 and is calculated at the median 3σ depth of the WISP fields presented in this paper, $f = 3.6 \times 10^{-17}$ erg s^{-1} cm^{-2}. At $z = 7.25$, this corresponds to $L_{Ly\alpha} = 2.2 \times 10^{43}$ erg s^{-1}.

The highly uncertain cumulative LF at $z = 7.3$ from Konno et al. (2014) is plotted in black. The gray symbols show the number densities of LAEs at $z \gtrsim 7$, including Iye et al. (2006) at $z = 6.96$, Ota et al. (2010) at $z = 7$, Vanzella et al. (2011) at $z = 7.008$ and 7.109, and Shibuya et al. (2012) at $z = 7.215$. These number densities are as presented by Faisst et al. (2014), where the authors have accounted for the different cosmologies and corrections used in the individual surveys. The black

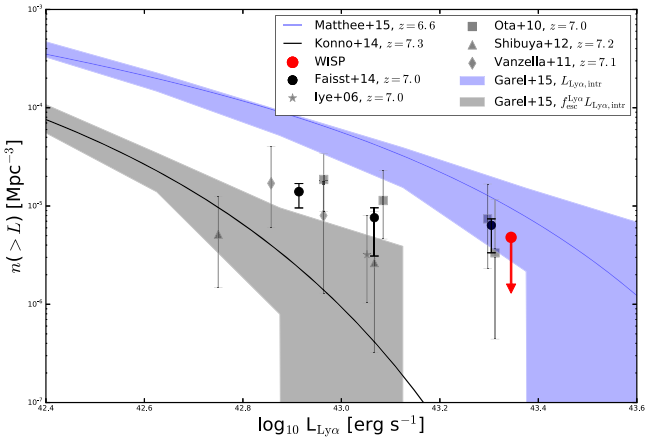

Figure 12. Cumulative number densities of LAEs at $z \sim 7$. The red arrow shows the WISP upper limit calculated from the volume probed over the redshift range $7 \leqslant z \leqslant 7.63$. The gray symbols show the number densities of LAEs from other surveys at $z \gtrsim 7$. The cumulative LFs of Konno et al. (2014) at z = 7.3 and Matthee et al. (2015) at z = 6.6 for reference are plotted in black and light blue, respectively. The shaded regions are the same as those plotted in Figure 9, but are calculated at these higher redshifts.

circles show the weighted median that Faisst et al. (2014) calculate for these $z \geqslant 7$ surveys.

The WISP limit is consistent with the other $z \sim 7$ measurements. Comparing this upper limit with the number density of the WISP $z \sim 6.4$ LAEs and the $z = 6.6$ Matthee et al. (2015) LF, we again find evidence for a decrease in the number density of LAEs from $z \sim 6.5$ to $z \gtrsim 7$. This drop could be due to a higher neutral hydrogen fraction in the IGM. However, it could also at least in part be due to an evolution in the intrinsic properties of galaxies at these redshifts, such as in the escape fraction of Lyα photons (e.g., Dijkstra et al. 2014).

As in Figure 9, the shaded regions in Figure 12 show the 1σ dispersions of the Lyα LFs measured from 100 realizations of mock light cones. While still within the region corresponding to galaxies with $f_{\rm esc}^{Ly\alpha} = 1$, the WISP point is of course an upper limit.

6.3. Extent of Lyα Halos

The detection, or lack thereof, of extended Lyα emission around a galaxy can provide important information about the presence and properties of its surrounding neutral hydrogen. Lyα photons may escape from a galaxy if they have been redshifted out of resonance by scattering through a shell of expanding material (e.g., Verhamme et al. 2006). The scattering process acts to diffuse the Lyα photons outward from their point of origin. The extent of the resulting Lyα halo is an indirect probe of the fraction of neutral hydrogen present around the galaxy. Extended emission is expected to be common around galaxies surrounded by partially or mostly neutral hydrogen, while more compact emission is expected when the surrounding hydrogen is ionized (and therefore scattering is minimized). Extended Lyα emission has been detected at redshifts in the range $z \sim 0.03$–6. The 14 well-studied galaxies in the Lyα Reference Sample (LARS; Hayes et al. 2013, 2014; Östlin et al. 2014) have Lyα emission that is ~3 times more extended than either their Hα or FUV emission. At $z = 2.2$, Momose et al. (2016) find scale lengths of Lyα halos ranging from 7 to 16 kpc, while Steidel et al. (2011) find evidence for Lyα halos extending out as far as 80 kpc at $z = 2.6$. At $z \sim 3.1$, Matsuda et al. (2012) detect Lyα halos out

to $\geqslant$60 kpc. Wisotzki et al. (2016) study a sample of galaxies at $3 \leqslant z \leqslant 6$ and find the Lyα emission is more extended than the UV by a factor of 5–10. On the other hand, compact Lyα emission has been observed at both intermediate and high redshifts: $z \simeq 2.1, 3.1$ (Feldmeier et al. 2013); and $z \simeq 5.7, 6.5$ (Jiang et al. 2013). The observed compact emission could indicate that the galaxies at these redshifts are surrounded by highly ionized hydrogen, even at the end of reionization at $z \sim 6.5$.

It is likely, however, that measurements of compact Lyα emission such as those of Feldmeier et al. (2013) and Jiang et al. (2013) reflect the surface brightness limits of the observations (e.g., Steidel et al. 2011; Schmidt et al. 2016; Wisotzki et al. 2016) rather then the physical environments surrounding the galaxies. Guaita et al. (2015) redshift LARS galaxies to simulate observations of these galaxies at $z \sim 2$ and $z \sim 5.7$. By $z = 5.7$, the extended Lyα emission is only detected in stacked narrowband images, and the stacked Lyα profile drops below the surface brightness limit at $\sim$5 kpc. Repeating this process for galaxies at $z = 7.2$ for the Grism Lens-Amplified Survey from Space (GLASS), Schmidt et al. (2016) find that the surface brightness of the extended Lyα emission in LARS galaxies is too faint to be detected in their stacked spectra.

Both LARS and GLASS reach depths comparable to or slightly deeper than WISP: 3×10^{-18} erg s^{-1} cm^{-2} in the $z = 5.7$ simulated LARS spectra and $(3.5 - 5) \times 10^{-18}$ erg s^{-1} cm^{-2} (observed, uncorrected for magnification) in the GLASS spectra. The WISP spectra are therefore only sensitive to the central, high-surface-brightness core of the Lyα emission. Indeed, the 1σ G_{102} depths reached in the two WISP fields are 5.5×10^{-17} erg s^{-1} cm^{-2} arcsec^{-2}, a factor of 550 times brighter than that reached by Wisotzki et al. (2016). We therefore do not draw conclusions from the compact Lyα profiles we measure. Instead, we suggest that the LAEs presented here are good candidates for targeted, deep follow-up observations aimed at exploring the extent of the Lyα halo at $z \sim 6.5$.

6.4. Ionized Bubbles

It is instructive to compare the observed Lyα luminosities with the intrinsic one, computed with basic assumptions on the stellar population of the WISP LAEs. We consider a range of parameters, including both Chabrier (2003) and Salpeter (1955) IMFs, metallicities of $Z/Z_{\odot} = 0.005$, 0.02 and 0.2, and ages from 10 Myr to 1 Gyr. Assuming Case B recombination, $n_e = 100$ cm^{-3}, and $T_e = 10^4$ K, the intrinsic Lyα luminosity of a galaxy can be estimated from the production rate of ionizing photons as (e.g., Schaerer 2003)

$$L_{\mathrm{Ly}\alpha,\mathrm{intr}} = C\ (1 - f_{\mathrm{esc}})\ N\gamma, \quad (6)$$

where $C = 1.04 \times 10^{-11}$ erg, and f_{esc} is the escape fraction of ionizing photons. Note that $N\gamma$ can be computed by scaling the stellar population model to the observed H_{160} magnitude (rest-frame 2000 Å, not contaminated by the Lyα emission). For reference, we adopt $f_{\mathrm{esc}} = 0$ and perform this calculation for *WISP302* only, since *WISP368* is undetected in the H_{160} continuum.

According to this model, and assuming the lowest metallicity covered by the BC03 models ($Z = 0.005 Z_{\odot}$) and an age of 10 Myr, *WISP302* can produce 5.1×10^{54} ionizing photons per second. The ratio of observed to intrinsic Lyα emission is therefore $\sim$0.9, implying that we are detecting almost all of the Lyα photons produced by this galaxy. More moderate parameter values result in an observed $L_{\mathrm{Ly}\alpha,\mathrm{obs}}$ that is greater than the intrinsic $L_{\mathrm{Ly}\alpha,\mathrm{intr}}$. Only models with a very young age and low metallicity produce a ratio $L_{\mathrm{Ly}\alpha,\mathrm{obs}}/L_{\mathrm{Ly}\alpha,\mathrm{intr}} < 1$.

This exercise suggests that these photons are not only able to escape from the galaxy's interstellar medium (ISM), but they are also not substantially attenuated by the surrounding IGM. In fact, local (i.e., where the IGM is not affecting the Lyα profile) analogs to high-z galaxies with large escape fractions of Lyα radiation are characterized by an emission line profile showing substantial flux blueward and close to the systemic velocity (Henry et al. 2015; Verhamme et al. 2015). The neutral IGM at $z \sim 6.5$ would attenuate this blue emission considerably, causing $L_{\mathrm{Ly}\alpha,\mathrm{obs}}$ / $L_{\mathrm{Ly}\alpha,\mathrm{intr}} \lesssim 0.5$. Hence, we conclude that a sizable neutral fraction in the presence of this galaxy is unlikely. This conclusion is also supported by the agreement between the LF calculated from the intrinsic Lyα emission (Garel et al. 2015) and the high number density of WISP LAEs (see Figure 9).

It is possible that the stellar population of *WISP302* is more extreme than our simple assumption. Both Pop III stars and models that include binaries have effectively harder spectra than typical Pop II stars and can produce a factor of up to $\sim$3 more ionizing photons than the spectral template discussed above (Schaerer 2002; Eldridge et al. 2008). A larger $L_{\mathrm{Ly}\alpha,\mathrm{intr}}$ would imply a much lower $L_{\mathrm{Ly}\alpha,\mathrm{obs}}/L_{\mathrm{Ly}\alpha,\mathrm{intr}}$ ratio, removing the need for a fully ionized IGM around this object. We can search for evidence of extreme stellar populations in *WISP302* by looking for the He II λ1640 Å emission line (Panagia 2005; Stanway et al. 2016) as well as other UV nebular emission lines (e.g., Stark et al. 2014).

The presence of dust could also reduce the $L_{\mathrm{Ly}\alpha,\mathrm{obs}}/L_{\mathrm{Ly}\alpha,\mathrm{intr}}$ ratio. If dust were present, $L_{\mathrm{Ly}\alpha,\mathrm{intr}}$ would be higher than what we estimate from our simple dust-free model. At the absolute magnitude of *WISP302*, however, Bouwens et al. (2016) show that the correction for dust extinction is negligible ($<$0.2 magnitude). As we cannot reliably measure the UV slope β, we rely on this estimate of dust extinction.

If extreme stars are not important, then the high $L_{\mathrm{Ly}\alpha,\mathrm{obs}}/L_{\mathrm{Ly}\alpha,\mathrm{intr}}$ ratio indicates that the IGM is mostly ionized around this galaxy. The current measurement of the Thomson optical depth from the cosmic microwave background radiation would allow for an end of the reionization process by as early as $z \sim 6.5$ (Robertson et al. 2015; Planck Collaboration et al. 2016a). However, if this were the case, we would expect bright galaxies such as the WISP LAEs to be more common. Therefore, it is more likely that objects like *WISP302* reside in rare, localized bubbles of ionized gas.

We now investigate the sources that are needed to create a sufficiently large ionized bubble for the Lyα emission to escape the effects of the IGM damping wing. Lyα photons will be transmitted through the IGM if the optical depth they experience is $\tau_{\mathrm{IGM}} < 1$. Miralda-Escudé (1998) shows that the minimum radius required is $R_{\mathrm{min}} \sim 1.216$ proper Mpc. Following Cen & Haiman (2000), we can define R_{max}, the maximum radius ionized over the course of *WISP302*'s lifetime, as

$$R_{\mathrm{max}} = \left(\frac{3\ N_{\mathrm{ion}}}{4\ \pi\ \langle n_{\mathrm{H}} \rangle} \right)^{1/3}. \quad (7)$$

Here, $\langle n_{\mathrm{H}} \rangle$ is the mean hydrogen density within R_{max}, and N_{ion} is the total number of ionizing photons emitted. Note that N_{ion} can

be expressed as the product of the rate of ionizing photons produced by the galaxy, the fraction of these that escape, and the galaxy's lifetime: $N_{\rm ion} = N_\gamma\, f_{\rm esc}\, t$. We assume the same stellar population as above, but we consider a longer star formation episode (i.e., $t = 100$ Myr). This age will provide us with a conservative upper limit on the radius of the ionized region.

Following Stiavelli (2009), we calculate the hydrogen number density from the mean density of a virialized halo, $\rho_{\rm vir}$:

$$\rho_{\rm vir} = \xi\ \Omega_M\ \rho_0\ (1+z)^3$$
$$n_{\rm H} = \frac{\rho_{\rm vir}\ \Omega_b}{\mu\ m_{\rm p}\ \Omega_M}, \quad (8)$$

where $\xi \simeq 178$ is the ratio between the density of a virialized system and the matter density of the universe, $\mu \simeq 1.35$ is the mean gas mass per hydrogen atom and accounts for the contribution of helium, $m_{\rm p}$ is the mass of a proton, and we adopt $\Omega_b h^2 = 0.0223$ (Planck Collaboration et al. 2016b). We find $R_{\rm max} \simeq 0.45 (f_{\rm esc})^{1/3}$ Mpc. Even if all of the ionizing photons escaped the galaxy's ISM ($f_{\rm esc} = 1$), the size would still be less than half of the minimum required radius, $R_{\rm min}$.

Clearly, *WISP302* is not capable of ionizing a large enough bubble on its own. We consider two alternative sources for the needed ionizing photons: a population of faint galaxies, as in Vanzella et al. (2011) and Castellano et al. (2016), or a bright quasar close to the studied LAE but outside the WISP field of view.

We begin with the first possibility. From Equation (7) we find that at least 1.45×10^{57} photons s^{-1} are required to create a sufficiently large ionized bubble, where we have assumed an escape fraction of $f_{\rm esc} = 0.1$. We next determine how many galaxies are needed to produce the required number of photons. To do so, we find the Lyα luminosity density by integrating

$$\int L\ \phi(L)\ dL, \quad (9)$$

where $\phi(L)dL$ is the LF, and we normalize by the observed number density of WISP LAEs. We then convert the Lyα luminosity density to a density of ionizing photons using Equation (6). Faint galaxies are the dominant source of ionizing photons, so we assume a simple power law LF and begin by considering a slope of $\alpha = -1.5$, matching the slopes plotted in Figure 9. In order to reach the requisite 10^{57} photons s^{-1}, we must integrate Equation (9) down to $L_{{\rm Ly}\alpha} \sim 0.001 L^*_{{\rm Ly}\alpha}$. This luminosity limit is on par with the minimum UV luminosities adopted by, for example, Robertson et al. (2015) and Rutkowski et al. (2016) in evaluating the contribution of star-forming galaxies to reionization. If we allow for a steeper faint-end slope such as $-2.3 < \alpha < -2.0$ (e.g., Dressler et al. 2015), we need only integrate down to $L_{{\rm Ly}\alpha} \sim 0.04 - 0.1 L^*_{{\rm Ly}\alpha}$. A substantial, but not unreasonable, number of faint galaxies is required to produce 10^{57} ionizing photons in the volume. Alternatively, in the presence of an overdensity, an increase in the LF normalization could further relax the need for faint galaxies. These calculations strongly depend on the escape fraction of Lyman continuum photons in these high-z galaxies (e.g., Rutkowski et al. 2016; Smith et al. 2016; Vanzella et al. 2016).

We now consider the second possibility that *WISP302* resides in a bubble ionized by a nearby quasar. For the same UV luminosity, quasars produce approximately an order of magnitude more ionizing photons than do star-forming galaxies. Moreover, the escape fraction of ionizing radiation is likely close to 100% (e.g., Loeb & Barkana 2001; Cristiani et al. 2016). For a single QSO to produce the required number of ionizing photons, it would need to be as bright as $H_{160} \sim 22$, not unreasonable given the luminosities of $z > 6$ QSOs observed by Fan et al. (2006). This object would be easily identified in the WISP survey, although none is detected in the region observed around *WISP302*. At $z = 6.4$, however, 1 Mpc corresponds to $\sim 3'$. Thus, it is possible that the quasar falls outside the WFC3 field. At this redshift, the average baryonic density of the universe is such that the recombination time is of the order of the age of the universe and shorter than typical QSO lifetimes (Trainor & Steidel 2013). Once ionized, the bubble could then remain ionized after the QSO has turned off. Imaging and spectroscopy over a wider area around *WISP302* are needed to investigate these possibilities.

7. Summary

In this paper we present the results of a search for $z > 6$ LAEs in the WISP survey. We find two $z \sim 6.5$ LAEs in $\sim$160 arcmin^2, probing a volume of 5.8×10^5 Mpc^3. We estimate the contamination fraction in our sample selection to be $\lesssim$2%, owing mainly to rare [O III] emitters at $z \sim 0.8$ with Hα/[O III] $<$0.25.

Our number density of bright WISP LAEs at $z \sim 6.5$ is higher than the previously reported measurements by Hu et al. (2010), Ouchi et al. (2010), and Kashikawa et al. (2011) and is consistent with the findings of Matthee et al. (2015). The discrepancy between the WISP measurement and these studies is likely due to a combination of our larger redshift coverage (and therefore comparable or even larger volume) and the almost negligible effect of cosmic variance in our sample.

We do not detect any $z > 7$ LAEs, and we determine that the $z = 6.6$ Lyα LF as measured by Matthee et al. (2015) must evolve from $z = 6.6$ to $z > 7$. Based on the expected number counts at the median depth of our fields, we cannot make a similar claim for the other $z \sim 6.5$ LFs. Our upper limit on the observed number density of LAEs in the WISP volume at $7 \leqslant z \leqslant 7.63$ is consistent with other $z \sim 7$ measurements.

We argue that the WISP LAEs reside in large ionized bubbles in the IGM. Using simple assumptions on their stellar populations, we conclude that they are not capable of ionizing their surroundings. We suggest that either a nearby bright quasar or a substantial population of fainter galaxies is required.

The WISP LAEs are excellent targets for studies of the IGM toward the end of reionization as well as the sources contributing to the ionizing photon budget. Follow-up observations can explore whether there is evidence for extreme stellar populations in these galaxies by targeting the He II emission line as well as other UV nebular emission lines (e.g., Stark et al. 2014). We can look for the presence of a blue wing in the Lyα line profile and obtain deep spectroscopic observations to investigate the absence (presence) of low surface brightness components around our LAEs to support (refute) the idea that these sources are located in ionized bubbles. Measurements of the LAEs' systemic velocities are also needed to determine whether the Lyα emission is close to the systemic velocity, as observed in some local galaxies with large Lyα escape fractions, or substantially redshifted. We note, however, that both the ISM and IGM can contribute to the redshifting of the line, and these contributions cannot be separated at these high redshifts.

Table 3
Luminosity Functions Used in Synthetic Catalog

Redshift	M^*_{UV} [a]	$\phi^*(10^{-3}$ Mpc $^{-3})$	α	Reference
$0.1 \leqslant z < 0.6$	-21.03 ± 0.25	5.0 ± 0.6	-1.26 ± 0.15	Scarlata et al. (2007)
$0.6 \leqslant z < 1.5$	-21.24 ± 0.12	4.9 ± 0.3	-1.22 ± 0.10	Scarlata et al. (2007)[b]
$1.5 \leqslant z < 2.7$	-20.01 ± 0.24	2.54 ± 0.15	-1.74 ± 0.08	Alavi et al. (2014)
$2.7 \leqslant z < 3.4$	-20.97 ± 0.14	1.71 ± 0.53	-1.73 ± 0.13	Reddy & Steidel (2009)
$3.4 \leqslant z < 4.5$	-20.88 ± 0.08	$1.97^{+0.34}_{-0.29}$	-1.64 ± 0.04	Bouwens et al. (2015)
$4.5 \leqslant z < 5.5$	-21.17 ± 0.12	$0.74^{+0.18}_{-0.14}$	-1.76 ± 0.05	Bouwens et al. (2015)
$5.5 \leqslant z < 6.5$	-20.94 ± 0.20	$0.5^{+0.22}_{-0.16}$	-1.87 ± 0.10	Bouwens et al. (2015)
$6.5 \leqslant z < 7.5$	-20.77 ± 0.28	$0.34^{+0.24}_{-0.14}$	-2.03 ± 0.13	Bouwens et al. (2015)
$7.5 \leqslant z \leqslant 8.5$	-20.21 ± 0.33	$0.45^{+0.42}_{-0.21}$	-1.83 ± 0.25	Bouwens et al. (2015)

Notes.
[a] Values of M^*_{UV} are derived at the rest-frame wavelengths of the B-band 4420 Å for $0.1 \leqslant z < 1.5$, 1500 Å for $1.5 \leqslant z < 2.7$, 1700 Å for $2.7 \leqslant z < 3.4$, and 1600 Å for $3.4 \leqslant z \leqslant 8.5$.
[b] LF is calculated for $0.6 \leqslant z \leqslant 0.8$ but here has been extended down to $z = 0.1$ and up to $z = 1.5$.

We can observe a wider field of view to search the surrounding volume for bright quasars or probe down to fainter Lyα luminosities to study the population of fainter galaxies around the bright LAEs. These observations can provide information on the sources mainly responsible for ionizing the regions around the LAEs. Follow-up observations can confirm whether there really are sufficient galaxies to create the bubbles, or whether a more powerful source of ionizing photons is required.

Finally, upcoming space-based dark energy missions have the potential to discover thousands of these bright LAEs. For example, covering 40 degrees^2 at a 3.5σ sensitivity of 6×10^{-17} erg s^{-1} cm^{-2}, the Euclid Deep Survey (Laureijs et al. 2012) has the potential to identify $\sim$70 LAEs per sq. degree at $6.5 \lesssim z \lesssim 7.0$. These targets would be ideal for ground-based and *JWST* follow-up.

We thank the anonymous referee for a careful review and suggestions that improved the manuscript. This research was partially supported by NASA ROSES grant 12-EUCLID12-0004. Support for *HST* Programs GO-11696, 12283, 12568, 12902, 13517, 13352, and 14178 was provided by NASA through grants from the Space Telescope Science Institute, which is operated by the Association of Universities for Research in Astronomy, Inc., under NASA contract NAS5-26555. T.G. is grateful to the LABEX Lyon Institute of Origins (ANR-10-LABX-0066) of the Université de Lyon for its financial support within the program "Investissements d'Avenir" (ANR-11-IDEX-0007) of the French government operated by the National Research Agency (ANR). This research has made use of NASA's Astrophysics Data System Bibliographic Services.

Appendix A
Simulated Template Library

For the purposes of deriving the optimal color selection for $z \geqslant 6$ galaxies, we generate a catalog of 20,000 synthetic sources based on the models of Bruzual & Charlot (2003, hereafter BC03). The catalog will be used to determine the broadband colors of galaxies with a variety of properties. We will therefore be calculating the mean flux density of each template spectrum in the four WFC3 filters used in this paper. Strong emission lines that fall within a filter passband can contribute significantly to the photometry, as much as 0.75 magnitudes or more, and can therefore have a large impact on broadband colors (e.g., Atek et al. 2011). In order to account for this effect in our synthetic catalog, we add emission lines to exactly half of the 20,000 templates. In what follows, we describe the templates and their properties in more detail. Unless otherwise noted, all properties—redshift, metallicity, star formation history, dust content, and so on—are drawn randomly from uniform distributions.

The template redshifts are in the range $0.1 \leqslant z \leqslant 8.5$. The luminosities of the synthetic sources in each redshift bin are distributed according to the LF at that redshift. To achieve this, in each of eight redshift bins, we integrate the appropriate LF down to a luminosity that corresponds to the 1σ magnitude limit of our survey and assign each source a luminosity extracted from this cumulative LF. Table 3 lists the LFs used in each redshift bin.

Each source is then assigned a spectral template extracted from a library of BC03 templates. We allow for either Chabrier (2003) or Salpeter (1955) initial mass functions, composite stellar populations of constant metallicity ($Z/Z_\odot = 0.005$, 0.02, 0.2, 0.4, or 1), and exponentially declining star formation histories (SFH) with characteristic timescales of $\tau = 0.01$, 0.5, and 5.0 Gyr. The timescales considered here approach those of models with, at either extreme, a constant SFH (large $\tau = 5$) and a single burst of star formation (small τ). We restrict the template metallicity with redshift such that the maximum possible metallicity (in units of $Z_\odot$) is $Z \leqslant 0.4$ at $1 < z \leqslant 2$, $Z \leqslant 0.2$ at $2 < z \leqslant 3$, and $Z \leqslant 0.02$ for $z > 3$. The full metallicity range is available for synthetic galaxies at $z \leqslant 1$. The spectra are extracted from these templates in logarithmic time steps such that the spectral evolution is better sampled for younger ages. Sources are then randomly assigned an age ranging from 10 Myr to the age of the universe at the given redshift.

When adding emission lines to the templates, the line luminosity for Hβ is determined from the flux of hydrogen-ionizing photons output by the BC03 models. Emission line coefficients for Hα and Lyα are from Table 1 of Schaerer (2003). We assume a Lyα escape fraction of $f_{esc}^{Ly\alpha} = 1$. The ratios of other rest-frame optical emission lines, relative to Hβ, depend on each template's metallicity, the electron temperature, and the electron density. We assume $n_e = 100$ cm^{-3} and $T_e = 10000$ K and take the resulting ratios from Anders & Fritze-v. Alvensleben (2003).

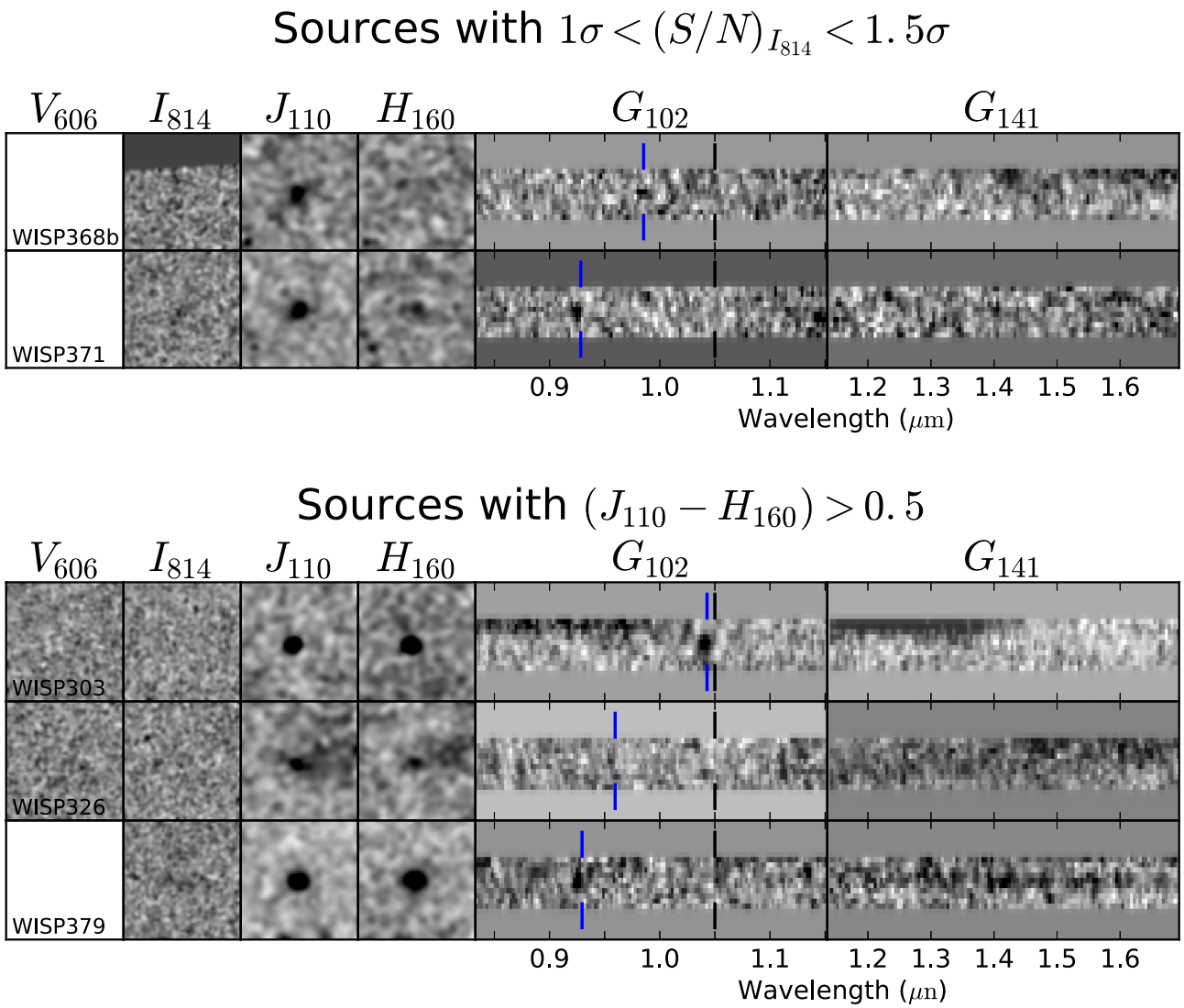

Figure 13. Direct image postage stamps and the two-dimensional spectral stamps of sources rejected from the LAE sample because of their flux in I_{814} (top) or their red ($J_{110} - H_{160}$) colors (bottom). Columns show, from left to right, V_{606}, I_{814}, J_{110}, H_{160}, G_{102}, and G_{141}. The postage stamps are 3″ on a side with the same pixel scales and smoothing kernels as those of Figure 5. The grism spectral stamps have been smoothed by the same kernel as that of Figure 6. In the G_{102} stamps, the black lines indicate the maximum wavelength cutoff of our criteria, $\lambda_{\rm obs} = 1.05\ \mu$m. The blue lines indicate the wavelength of the emission line.

These templates of stellar and nebular emission are next reddened using two distinct dust geometries (see Scarlata et al. 2009): (1) a uniform slab of dust in front of the source, and (2) a clumpy slab in front of an extended source. In the first case, extinction follows the classical $I_o/I_i = e^{-\tau_\lambda}$, where I_o and I_i are the observed and intrinsic intensities, respectively, and $\tau_\lambda = \kappa_\lambda\ E(B-V)/1.086$. We use the Calzetti et al. (2000) reddening curve for κ_λ, with color excess values in the stellar continuum drawn randomly from a uniform distribution of $0 < E_s(B-V) < 1$. For the second model, we assume all clumps have the same optical depths, $\tau_{c,\lambda}$, and they are distributed according to a Poisson distribution with a mean equal to the average number of clumps along the line of sight, N. The number of clumps is randomly drawn from a uniform distribution of $1 \leqslant N \leqslant 10$. We assign each clump an optical depth in the V band such that $0.1 \leqslant \tau_{c,V} \leqslant 10$. Each clump acts as a uniform dust screen and follows the Cardelli et al. (1989) extinction law. The ISM extinction then goes as $I_o/I_i = \exp[-N(1 - e^{-\tau_{c,\lambda}})]$ (Natta & Panagia 1984). We randomly assign one of the two dust geometries to each template. Assuming the dust content of the universe decreases exponentially with increasing redshift, we restrict the maximum available extinction E_{B-V} (either in the uniform ISM or in the clumps) following Hayes et al. (2011), where $E_{B-V}(z) = C_{EBV}\ \exp(z/z_{EBV})$, $C_{EBV} = 0.386$, and $z_{EBV} = 3.42$.

The reddened spectra are then attenuated by the neutral hydrogen in the IGM using the recipe from Inoue et al. (2014), which is an updated version of the Madau (1995) attenuation model. Inoue et al. (2014) include absorption from the full Lyman series, Lyman limit systems, and damped Lyα systems, as well as a more accurate representation of absorption in the Lyman continuum.

For each simulated galaxy, we compute the V_{606}, I_{814}, J_{110}, and H_{160} magnitudes. Finally, we add errors to the synthetic magnitudes to account for the photometric uncertainties in our observed catalog. Photometric scatter is one of the dominant causes of contamination in Lyman break samples (e.g., Stanway et al. 2008). It operates in both directions, scattering galaxies both into and out of the selection window, thus affecting both the contamination and recovery fractions.

Table 4
Additional Sources

ID	R.A. (J2000)	Decl. (J2000)	$f_{\rm line}$ (10^{-17} erg s^{-1} cm^{-2})	V_{606} (mag)	I_{814} (mag)	J_{110} (mag)	$f_{J110}^{\rm neb}/f_{J110}^{\rm total}$	H_{160} (mag)
WISP368b	23:22:35.32	−34:50:41.6	6.1 ± 1.2	···	27.6 ± 0.7	26.6 ± 0.2	0.73	27.18 ± 0.8
WISP371	20:05:49.69	−41:39:38.6	7.2 ± 1.1	···	27.5 ± 0.6	26.0 ± 0.1	0.50	25.8 ± 0.3
WISP303	13:48:29.26	+26:32:44.3	5.5 ± 0.6	>28.26	>27.35	25.5 ± 0.1	0.24	24.8 ± 0.1
WISP326	05:30:03.91	−07:24:10.4	2.3 ± 0.6	>28.09	>27.55	25.8 ± 0.3	0.13	25.7 ± 0.2
WISP379	12:56:49.61	+56:52:48.5	6.9 ± 1.3	···	>27.97	25.5 ± 0.2	0.30	24.3 ± 0.2

We add photometric scatter to our synthetic catalog in the following way. From the WISP photometric catalog, we determine the average uncertainty as a function of magnitude for each filter. The magnitudes of the synthetic sources are then allowed to vary according to Gaussian distributions with standard deviations set by the median uncertainty in the corresponding magnitude bins. We create 10 such realizations of the synthetic photometry, resulting in a final catalog of 2×10^5 sources. This catalog is used in Section 3.1 to choose the selection criteria for $z > 6$ LAEs and also to characterize possible sources of contamination in the sample in Section 4.

Appendix B
Additional Sources

In Figure 13, we present the imaging and spectral stamps of two categories of sources that were conservatively excluded from the LAE sample. The top section shows sources that are marginally detected in I_{814} at the 1σ level. These galaxies have $1\sigma < (\mathrm{S/N})_{I_{814}} < 1.5\sigma$ and are discussed in Section 3.1.2. The bottom section shows sources that have IR colors that place them outside our color selection window: $(J_{110} - H_{160}) > 0.5$. These galaxies may be very dusty or have strong 4000 Å breaks. They are discussed in Section 5.2. Table 4 presents the emission line fluxes and photometry for these five objects.

References

Alavi, A., Siana, B., Richard, J., et al. 2014, ApJ, 780, 143
Anders, P., & Fritze-v. Alvensleben, U. 2003, A&A, 401, 1063
Atek, H., Malkan, M., McCarthy, P., et al. 2010, ApJ, 723, 104
Atek, H., Siana, B., Scarlata, C., et al. 2011, ApJ, 743, 121
Bertin, E., & Arnouts, S. 1996, A&AS, 117, 393
Bouwens, R., Aravena, M., Decarli, R., et al. 2016, ApJ, 833, 72
Bouwens, R. J., Illingworth, G. D., Oesch, P. A., et al. 2015, ApJ, 803, 34
Bruzual, G., & Charlot, S. 2003, MNRAS, 344, 1000
Calzetti, D., Armus, L., Bohlin, R. C., et al. 2000, ApJ, 533, 682
Cardelli, J. A., Clayton, G. C., & Mathis, J. S. 1989, ApJ, 345, 245
Castellano, M., Dayal, P., Pentericci, L., et al. 2016, ApJL, 818, L3
Cen, R., & Haiman, Z. 2000, ApJL, 542, L75
Chabrier, G. 2003, PASP, 115, 763
Colbert, J. W., Teplitz, H., Atek, H., et al. 2013, ApJ, 779, 34
Cristiani, S., Serrano, L. M., Fontanot, F., Vanzella, E., & Monaco, P. 2016, MNRAS, 462, 2478
Dickinson, M., Stern, D., Giavalisco, M., et al. 2004, ApJL, 600, L99
Dijkstra, M., Wyithe, S., Haiman, Z., Mesinger, A., & Pentericci, L. 2014, MNRAS, 440, 3309
Domínguez, A., Siana, B., Henry, A. L., et al. 2013, ApJ, 763, 145
Dressler, A., Henry, A., Martin, C. L., et al. 2015, ApJ, 806, 19
Dressler, A., Martin, C. L., Henry, A., Sawicki, M., & McCarthy, P. 2011, ApJ, 740, 71
Eldridge, J. J., Izzard, R. G., & Tout, C. A. 2008, MNRAS, 384, 1109
Faisst, A. L., Capak, P., Carollo, C. M., Scarlata, C., & Scoville, N. 2014, ApJ, 788, 87
Fan, X., Strauss, M. A., Becker, R. H., et al. 2006, AJ, 132, 117
Feldmeier, J. J., Hagen, A., Ciardullo, R., et al. 2013, ApJ, 776, 75
Felten, J. E. 1977, AJ, 82, 861
Froning, C. S., & Green, J. C. 2009, Ap&SS, 320, 181
Garel, T., Blaizot, J., Guiderdoni, B., et al. 2012, MNRAS, 422, 310
Garel, T., Blaizot, J., Guiderdoni, B., et al. 2015, MNRAS, 450, 1279
Gehrels, N. 1986, ApJ, 303, 336
Gonzaga, S., Hack, W., Fruchter, A., & Mack, J. (ed.) 2012, The DrizzlePac Handbook (Baltimore, MD: STScI)
Guaita, L., Melinder, J., Hayes, M., et al. 2015, A&A, 576, A51
Hayes, M., Östlin, G., Duval, F., et al. 2014, ApJ, 782, 6
Hayes, M., Östlin, G., Schaerer, D., et al. 2013, ApJL, 765, L27
Hayes, M., Schaerer, D., Östlin, G., et al. 2011, ApJ, 730, 8
Henry, A., Scarlata, C., Domínguez, A., et al. 2013, ApJL, 776, L27
Henry, A., Scarlata, C., Martin, C. L., & Erb, D. 2015, ApJ, 809, 19
Henry, A. L., Martin, C. L., Dressler, A., Sawicki, M., & McCarthy, P. 2012, ApJ, 744, 149
Henry, A. L., Siana, B., Malkan, M. A., et al. 2009, ApJ, 697, 1128
Hu, E. M., Cowie, L. L., Barger, A. J., et al. 2010, ApJ, 725, 394
Hu, E. M., Cowie, L. L., Songaila, A., et al. 2016, ApJL, 825, L7
Inoue, A. K., Shimizu, I., Iwata, I., & Tanaka, M. 2014, MNRAS, 442, 1805
Iye, M., Ota, K., Kashikawa, N., et al. 2006, Natur, 443, 186
Jiang, L., Egami, E., Fan, X., et al. 2013, ApJ, 773, 153
Kashikawa, N., Shimasaku, K., Matsuda, Y., et al. 2011, ApJ, 734, 119
Kimble, R. A., MacKenty, J. W., O'Connell, R. W., & Townsend, J. A. 2008, Proc. SPIE, 7010, 70101E
Kimble, R. A., Woodgate, B. E., Bowers, C. W., et al. 1998, ApJL, 492, L83
Konno, A., Ouchi, M., Nakajima, K., et al. 2016, ApJ, 823, 20
Konno, A., Ouchi, M., Ono, Y., et al. 2014, ApJ, 797, 16
Krug, H. B., Veilleux, S., Tilvi, V., et al. 2012, ApJ, 745, 122
Kümmel, M., Walsh, J. R., Pirzkal, N., Kuntschner, H., & Pasquali, A. 2009, PASP, 121, 59
Laureijs, R., Gondoin, P., Duvet, L., et al. 2012, Proc. SPIE, 8442, 84420T
Loeb, A., & Barkana, R. 2001, ARA&A, 39, 19
Madau, P. 1995, ApJ, 441, 18
Madau, P., & Haardt, F. 2015, ApJL, 813, L8
Maiolino, R., Nagao, T., Grazian, A., et al. 2008, A&A, 488, 463
Matsuda, Y., Yamada, T., Hayashino, T., et al. 2012, MNRAS, 425, 878
Matthee, J., Sobral, D., Santos, S., et al. 2015, MNRAS, 451, 400
Matthee, J. J. A., Sobral, D., Swinbank, A. M., et al. 2014, MNRAS, 440, 2375
McQuinn, M., Hernquist, L., Zaldarriaga, M., & Dutta, S. 2007, MNRAS, 381, 75
Mehta, V., Scarlata, C., Colbert, J. W., et al. 2015, ApJ, 811, 141
Mesinger, A., & Furlanetto, S. R. 2008, MNRAS, 385, 1348
Miralda-Escudé, J. 1998, ApJ, 501, 15
Mobasher, B., Dickinson, M., Ferguson, H. C., et al. 2005, ApJ, 635, 832
Momose, R., Ouchi, M., Nakajima, K., et al. 2014, MNRAS, 442, 110
Momose, R., Ouchi, M., Nakajima, K., et al. 2016, MNRAS, 457, 2318
Natta, A., & Panagia, N. 1984, ApJ, 287, 228
Oesch, P. A., Bouwens, R. J., Illingworth, G. D., et al. 2010, ApJL, 709, L16
Oke, J. B., & Gunn, J. E. 1983, ApJ, 266, 713
Ono, Y., Ouchi, M., Mobasher, B., et al. 2012, ApJ, 744, 83
Östlin, G., Hayes, M., Duval, F., et al. 2014, ApJ, 797, 11
Ota, K., Iye, M., Kashikawa, N., et al. 2010, ApJ, 722, 803
Ouchi, M., Shimasaku, K., Akiyama, M., et al. 2008, ApJS, 176, 301
Ouchi, M., Shimasaku, K., Furusawa, H., et al. 2010, ApJ, 723, 869
Panagia, N. 2005, in The Initial Mass Function 50 Years Later, ed. E. Corbelli, F. Palla, & H. Zinnecker (Dordrecht: Springer), 479
Pentericci, L., Fontana, A., Vanzella, E., et al. 2011, ApJ, 743, 132
Pentericci, L., Vanzella, E., Fontana, A., et al. 2014, ApJ, 793, 113
Pirzkal, N., Rothberg, B., Ryan, R., et al. 2013, ApJ, 775, 11
Planck Collaboration, Adam, R., Aghanim, N., et al. 2016a, A&A, 596, A108
Planck Collaboration, Ade, P. A. R., Aghanim, N., et al. 2016b, A&A, 594, A13

Rafelski, M., Teplitz, H. I., Gardner, J. P., et al. 2015, AJ, 150, 31
Reddy, N. A., & Steidel, C. C. 2009, ApJ, 692, 778
Roberts-Borsani, G. W., Bouwens, R. J., Oesch, P. A., et al. 2016, ApJ, 823, 143
Robertson, B. E., & Ellis, R. S. 2012, ApJ, 744, 95
Robertson, B. E., Ellis, R. S., Furlanetto, S. R., & Dunlop, J. S. 2015, ApJL, 802, L19
Ross, N. R., Colbert, J., Malkan, A., et al. 2016, ApJ, submitted
Rutkowski, M. J., Scarlata, C., Haardt, F., et al. 2016, ApJ, 819, 81
Salpeter, E. E. 1955, ApJ, 121, 161
Santos, S., Sobral, D., & Matthee, J. 2016, MNRAS, 463, 1678
Scarlata, C., Carollo, C. M., Lilly, S., et al. 2007, ApJS, 172, 406
Scarlata, C., Colbert, J., Teplitz, H. I., et al. 2009, ApJL, 704, L98
Schaerer, D. 2002, A&A, 382, 28
Schaerer, D. 2003, A&A, 397, 527
Schaerer, D., Hayes, M., Verhamme, A., & Teyssier, R. 2011, A&A, 531, A12
Schenker, M. A., Robertson, B. E., Ellis, R. S., et al. 2013, ApJ, 768, 196
Schenker, M. A., Stark, D. P., Ellis, R. S., et al. 2012, ApJ, 744, 179
Schmidt, K. B., Treu, T., Bradač, M., et al. 2016, ApJ, 818, 38
Shibuya, T., Kashikawa, N., Ota, K., et al. 2012, ApJ, 752, 114
Smith, B. M., Windhorst, R. A., Jansen, R. A., et al. 2016, arXiv:1602.01555
Sobral, D., Matthee, J., Darvish, B., et al. 2015, ApJ, 808, 139
Stanway, E. R., Bremer, M. N., & Lehnert, M. D. 2008, MNRAS, 385, 493
Stanway, E. R., Eldridge, J. J., & Becker, G. D. 2016, MNRAS, 456, 485
Stark, D. P., Ellis, R. S., Charlot, S., et al. 2016, MNRAS, 464, 469
Stark, D. P., Richard, J., Charlot, S., et al. 2015, MNRAS, 450, 1846
Stark, D. P., Richard, J., Siana, B., et al. 2014, MNRAS, 445, 3200
Steidel, C. C., Bogosavljević, M., Shapley, A. E., et al. 2011, ApJ, 736, 160
Stiavelli, M. 2009, From First Light to Reionization: The End of the Dark Ages (Berlin: Wiley)
Tilvi, V., Rhoads, J. E., Hibon, P., et al. 2010, ApJ, 721, 1853
Trainor, R., & Steidel, C. C. 2013, ApJL, 775, L3
Trenti, M., & Stiavelli, M. 2008, ApJ, 676, 767
Treu, T., Trenti, M., Stiavelli, M., Auger, M. W., & Bradley, L. D. 2012, ApJ, 747, 27
Vanzella, E., de Barros, S., Vasei, K., et al. 2016, ApJ, 825, 41
Vanzella, E., Pentericci, L., Fontana, A., et al. 2011, ApJL, 730, L35
Verhamme, A., Orlitová, I., Schaerer, D., & Hayes, M. 2015, A&A, 578, A7
Verhamme, A., Schaerer, D., & Maselli, A. 2006, A&A, 460, 397
Wisotzki, L., Bacon, R., Blaizot, J., et al. 2016, A&A, 587, A98
Zheng, Z., Cen, R., Trac, H., & Miralda-Escudé, J. 2010, ApJ, 716, 574
Zheng, Z., Cen, R., Trac, H., & Miralda-Escudé, J. 2011, ApJ, 726, 38